Monthly Notices
of the
ROYAL ASTRONOMICAL SOCIETY

MNRAS **432,** 2150–2176 (2013)
Advance Access publication 2013 May 9

doi:10.1093/mnras/stt564

On the nature of the red, 2MASS-selected AGN in the local Universe I: an optical spectroscopic study

M. Rose,[1]⋆ C. N. Tadhunter,[1] J. Holt[2] and J. Rodríguez Zaurín[3]

[1]*Department of Physics and Astronomy, University of Sheffield, Sheffield S3 7RH, UK*
[2]*Leiden Observatory, Leiden University, PO Box 9513, NL-2300 RA Leiden, the Netherlands*
[3]*Instituto de Astrofisica de Canarias, E-38205, La Laguna (Tenerife), Spain*

Accepted 2013 March 27. Received 2013 February 18; in original form 2012 November 9

ABSTRACT

We present optical spectra for a representative sample of 27 nearby ($z < 0.2$) Two Micron All Sky Survey (2MASS)-selected active galactic nuclei (AGN) with red near-infrared colours ($J - K_S \gtrsim 2.0$). The spectra were taken with the ISIS spectrograph on the William Herschel Telescope with the aim of determining the nature of the red 2MASS AGN, in particular whether they are young quasars obscured by their natal cocoons of gas and dust. We compare our findings with those obtained for comparison samples of PG quasars and unobscured type 1 AGN. The spectra show a remarkable variety, including moderately reddened type 1 objects (45 per cent), type 1 objects that appear similar to traditional ultraviolet (UV)-/optical-selected AGN (11 per cent), narrow-line type 1 Seyfert AGN (15 per cent), type 2 AGN (22 per cent) and H II/composite objects (7 per cent). The high Balmer decrements that we measure in many of the type 1 objects are consistent with their red $J - K_S$ colours being due to moderate levels of dust extinction ($0.2 < E(B - V) < 1.2$). However, we measure only modest velocity shifts and widths for the broader [O III]λ5007 emission-line components that are similar to those measured in the comparison samples. This suggests that the outflows in the red 2MASS objects are not unusual compared with those of optical-/UV-selected AGN of similar luminosity. In addition, the Eddington ratios for the 2MASS sample are relatively modest. Overall, based on their optical spectra, we find no clear evidence that the population of red, 2MASS-selected AGN at low redshifts represents young quasars. Most plausibly, these objects are normal type 1 AGN that are moderately obscured by material in the outer layers of the circumnuclear tori or in the discs of the host galaxies.

Key words: galaxies: active – quasars: emission lines – quasars: general – galaxies: Seyfert.

1 INTRODUCTION

Most of our understanding of active galactic nuclei (AGN) is based on samples of AGN detected in ultraviolet (UV)/optical surveys. Indeed, key advances such as measuring high cosmological redshifts (Hazard, Mackey & Shimmins 1963) and developing the orientation-based unified schemes (see Antonucci 1993) are based on the study of AGN at UV/optical wavelengths. However, there has been increasing evidence that a large fraction of AGN have not been detected in UV/optical surveys because they are obscured by large columns of dust (Webster et al. 1995; Cutri et al. 2002). Surveys at infrared (IR) and radio wavelengths suggest that up to 80 per cent of all AGN may have been missed in current UV/optical surveys (see Low et al. 1988; Webster et al. 1995; Francis, Whiting & Webster 1999).

A key result of the Two Micron All Sky Survey (2MASS) was the discovery of a population of AGN that appear redder than their traditional optical-/UV-selected counterparts at IR wavelengths. The red 2MASS AGN were selected to have $J - K_S \gtrsim 2.0$, distinguishing them from most optical-/UV-selected AGN that have bluer near-IR (NIR) colours ($J - K_S < 2.0$; Cutri et al. 2002), and K-band magnitudes in the range $11.0 < K_S < 14.9$ mag. The latter criterion was chosen so that bright ($K_S < 11.0$) Galactic asymptotic giant branch and carbon stars were excluded, along with 'normal' galaxies in the redshift range $0.4 < z < 0.5$ ($K_S > 14.9$; Cutri et al. 2002). Spectroscopic follow-up of the objects which fulfil these criteria revealed that the majority of the candidates have spectra resembling AGN (Cutri et al. 2002). More recent surveys have determined that these 'red quasars' do indeed represent a large fraction of the overall population of quasars in the local Universe (∼15–60 per cent; Glikman et al. 2007, 2012).

Because the red quasars potentially make up a large fraction of the AGN population, it is important that we understand their

⋆E-mail: m.rose@sheffield.ac.uk

relationship to the unobscured population: are they young, dust-obscured versions of 'typical quasars' (Hutchings et al. 2003; Georgakakis et al. 2009; Glikman et al. 2007, 2012)? Or can their properties be explained by a specific viewing angle in the orientation-based unified schemes (Wilkes et al. 2002)? Or do they perhaps represent a new population altogether? Are these objects all luminous quasars, or are some less luminous AGN?

Past studies of red 2MASS quasars have found reddenings in the range $0.1 < E(B-V) < 3.2$ magnitudes, based on Balmer decrements and fits to the continuum shape (e.g. Glikman et al. 2007, 2012; Georgakakis et al. 2009; Kuraszkiewicz et al. 2009a,b; Canalizo et al. 2012), although it is important to recognize that some have negligible reddening (Glikman et al. 2007). In addition, imaging studies of the host galaxies find evidence for disturbed morphologies in up to 70 per cent of cases (Hutchings et al. 2003; Marble et al. 2003; Urrutia, Lacy & Becker 2008), which may support the idea that host galaxies have undergone recent interactions with other galaxies. Such interactions could drive material into the central region of the galaxies, enshrouding the supermassive black hole (SMBH) in a cocoon of dust (Hopkins et al. 2006), making them difficult to detect in traditional UV/optical surveys (Cutri et al. 2002).

Many previous studies of 'red quasars' have focused on samples covering a wide range of redshift ($0 < z < 3$; Glikman et al. 2007, 2012; Georgakakis et al. 2009). The problem with such samples is that it is difficult to investigate the intrinsic diversity of the red quasar population in the face of possible evolutionary and/or luminosity-dependent effects. Therefore, it is important to study a sample of 2MASS-selected AGN that covers a more limited range in redshift.

This paper reports observations of a right ascension (RA)-limited sample of 27 2MASS-selected AGN ($J - K_S \gtrsim 2.0$) with a narrow range of redshifts: $0.09 < z < 0.20$. We aim to determine how the red 2MASS AGN fit into our picture of active galaxies in general, and how important they are to our understanding of AGN. In this, the first of two papers (Paper I), we report a spectroscopic study of the sample, focusing on the AGN properties, emission-line outflows and dust extinction. The spectral properties are compared to control samples of optical-/UV-selected quasars and AGN. Paper II in the series will focus on the NIR and mid-IR properties of the sample, and will include a comprehensive comparison with several complete samples of active galaxies.

The cosmological parameters used throughout this paper are adopted from *Wilkinson Microwave Anisotropy Probe*: $H_0 = 71$ km s^{-1}, $\Omega_M = 0.27$ and $\Omega_\Lambda = 0.73$ (Spergel et al. 2003).

2 OBSERVATIONS AND DATA REDUCTION

The full sample for this survey comprises a complete RA-limited ($2 < \mathrm{RA} < 15$ h) subsample of 27 objects with red NIR colours ($J - K_S \gtrsim 2$), K-band magnitudes in the range $11.0 < K_S < 14.9$ mag and redshifts $z < 0.2$, selected from the list of Hutchings et al. (2003), which is itself representative of the population of red, 2MASS-selected quasars. We also observed a further two objects from Hutchings et al. (2003) that fall outside the original redshift and/or RA range: J1637+25 ($z = 0.277$) and J2124−17 ($z = 0.111$). Therefore, the total sample consists of 29 objects; however, two of these objects have redshifts $z > 0.2$. Although we present the data for the full 29 objects, we only consider the results for the 27 objects with redshifts $z < 0.2$ in the analysis. Table 1 shows the basic properties of the sample.

Low-resolution optical spectroscopic observations of the sample were taken with the ISIS dual-arm spectrograph on the 4.2 m William Herschel Telescope (WHT) on La Palma in three runs: the 2006 July 28, 2007 February 8 and 9, and 2011 September 26 and 27. The data were taken with the ISIS dual-arm spectrograph on the WHT. On the red arm, the R158R grating was used with the REDPLUS CCD, and on the blue arm, the R300B grating was used with the EEV12 CCD. A dichroic cutting at 5300 Å was employed to obtain spectra simultaneously in the blue (∼3250–5250 Å) and in the red (∼5200–9500 Å). To reduce the effects of differential refraction, all exposures were taken when the objects were at low airmass (sec $z < 1.1$) and/or with the slit aligned close to the parallactic angle. The seeing for the nights of the observations varied over the range $0.8 < \mathrm{FWHM} < 1.3$ arcsec.

Sets of three exposures were taken on both arms simultaneously for each object using a 1.5 arcsec slit. An additional wider slit (5 arcsec) exposure was taken on both arms for 23 of the objects.[1] This was to assess the effect of possible slit losses on the emission-line flux. To eliminate contamination from second-order emission, a GG495 blocking filter was introduced into the ISIS red arm. The exposure times for each object are given in Table 1.

The data were reduced in the standard way (bias subtraction, flat fielding, cosmic ray removal, wavelength calibration and flux calibration) using packages in IRAF.[2] The 2D spectra were also corrected for spatial distortions. To reduce wavelength calibration errors due to flexure of the telescope and instrument, arc spectra were taken at the position of each object on the sky. Based on measurements of the night sky lines, the wavelength calibration uncertainties are 0.1 Å on both the blue and red arms, and the narrow slit spectral resolution is estimated to be ∼5.6 and ∼10.5 Å on the blue and red arms, respectively, for 23/29 of the objects, and ∼6.6 and ∼6.1 Å for the blue and red arms for the rest of the sample (see Table 1). Atmospheric absorption features were removed by dividing the red spectrum of each object by that of a telluric standard, taken close in time and airmass to the observations of 27/29 of the objects. No telluric standards were taken for J1637+25 and J2124−17, and therefore the atmospheric features were not removed for those objects. The spatial pixel scales of the 2D spectra are 0.4 arcsec in the blue and 0.44 arcsec in the red, and the relative flux calibration uncertainty – based on 11 observations of 8 flux standard stars taken throughout the runs – is estimated to be ±5 per cent.

The spectra were extracted and analysed using the Starlink packages FIGARO and DIPSO. All extracted spectra were corrected for Galactic extinction using the Galactic extinction maps of Schlegel, Finkbeiner & Davis (1998) and the extinction laws of Seaton (1979) for the UV, and Howarth (1983) for the optical/IR, prior to the analysis. In order to investigate the nuclear spectra, we extracted apertures centred on the nuclei of the targets in the 2D spectra, with aperture sizes chosen such that the full flux from the nucleus of each object was extracted. The aperture sizes are given in Table 1 and the extracted spectra are shown in Fig. 1.

[1] Wide slit exposures were not taken for six of the objects in the sample: J0221+13, J0248+14, J0306−05, J0312+07, J1637+25 and J2124−17. These objects were observed on separate runs to the rest of the sample.

[2] IRAF is distributed by the National Optical Astronomy Observatory, which is operated by the Association of Universities for the Research in Astronomy, Inc., under cooperative agreement with the National Science Foundation (http://iraf.noao.edu/).

Table 1. Basic properties of the 2MASS sample. The second column gives the abbreviated name used for each object in this paper. 'Type' gives the spectral type of the AGN. We only classify an object as type 1 if it shows significant (i.e. well above the noise) broad wings that cannot be accounted for by the [O III] model fitted to the Hα+[N II] lines. Redshifts and [O III] emission-line luminosities ($L_{[O\,III]}$) were determined using the [O III]λ5007 emission line, and $J - K_S$ values were taken from the 2MASS point source catalogue. The key for the 'Run' column is: (a) observed on 2007 February 8 and 9, (b) 2006 July 28 and (c) 2011 September 26 and 27.

Full object name	Name	Type	z	$J - K_S$	$L_{[O\,III]}$ (10^{34} W)	Run	Exp. time (s)	B/N slit ratio	Blue (Å)	Red (Å)	Aperture (arcsec^2)
J02215058+1327409	J0221+13	Type 2	$0.1402 \pm 0.000\,21$	2.37	0.76 ± 0.09	c	600	–	6.80	6.14	2.2×1.5
J02480733+1459577	J0248+14	Type 1	$0.0718 \pm 0.000\,24$	2.13	0.21 ± 0.02	c	300	–	6.87	6.35	2.2×1.5
J03065242−0531569	J0306−05	Type 2	$0.1261 \pm 0.000\,89$	2.24	0.95 ± 0.83	c	600	–	6.21	6.41	2.2×1.5
J03123105+0706547	J0312+07	Type 1	$0.1455 \pm 0.000\,33$	1.98	0.7 ± 0.03	c	600	–	6.57	6.51	1.76×1.5
J04001974+0502149	J0400+05	Type 1	$0.1876 \pm 0.000\,14$	2.00	22.39 ± 0.85	a	600	1.03 ± 0.13	5.02	10.50	2.2×1.5
J04092488+0758560	J0409+07	Type 1	$0.0914 \pm 0.000\,19$	2.17	3.67 ± 0.19	a	600	1.14 ± 0.37	5.26	10.13	1.76×1.5
J04112647−0118056	J0411−01	LINER/H II	0.1395 ± 0.0035	2.22	0.06 ± 0.02	a	600	1.13 ± 0.31	5.23	10.40	2.2×1.5
J04225654−1854424	J0422−18	Type 1	$0.0646 \pm 0.000\,18$	2.21	2.35 ± 0.03	a	300	1.08 ± 0.06	5.59	10.56	2.2×1.5
J04352254−0635256	J0435−06	Type 1	$0.1846 \pm 0.000\,74$	1.98	1.74 ± 0.07	a	600	1.87 ± 0.59	5.56	10.40	2.2×1.5
J04474760−1649344	J0447−16	Type 1	$0.1985 \pm 0.000\,92$	2.10	1.04 ± 0.11	a	600	0.85 ± 0.33	5.55	10.83	2.2×1.5
J05042569−1909258	J0504−19	Type 2	$0.1376 \pm 0.000\,92$	2.04	3.4 ± 0.04	a	450	1.00 ± 0.22	5.48	10.23	2.2×1.5
J091000.74+334809	J0910+33	Type 2	$0.1779 \pm 0.000\,21$	2.33	9.01 ± 0.28	a	600	1.15 ± 0.12	5.31	10.23	1.76×1.5
J100139.51+410423	J1001+41	LINER/H II	0.1427 ± 0.0021	2.00	0.11 ± 0.02	a	450	2.04 ± 0.36	5.71	10.94	1.76×1.5
J10065783+4104064	J1006+41	Type 1	$0.0890 \pm 0.000\,34$	1.92	1.99 ± 0.1	a	600	1.12 ± 0.48	5.17	10.54	1.76×1.5
J101400.47+194614	J1014+19	Type 1	$0.1112 \pm 0.000\,18$	2.04	8.7 ± 0.23	a	300	1.12 ± 0.11	5.56	10.80	2.2×1.5
J10404364+5934092	J1040+59	Type 1	$0.1476 \pm 0.000\,76$	3.02	0.98 ± 0.09	a	600	1.03 ± 0.36	5.33	10.24	2.2×1.5
J10572861−1353597	J1057−13	Type 2	0.1633 ± 0.0002	2.50	5.17 ± 0.18	a	600	1.22 ± 0.21	5.73	10.49	2.2×1.5
J11275114+2432081	J1127+24	Type 1	$0.1366 \pm 0.000\,21$	1.97	0.81 ± 0.01	a	500	1.15 ± 0.03	5.52	10.06	2.64×1.5
J113111.05+162739	J1131+16	Type 2	0.1732 ± 0.0001	2.15	10.02 ± 0.29	a	600	1.05 ± 0.12	6.11	11.37	1.76×1.5
J11582462−3003350	J1158−30	Type 2	$0.1352 \pm 0.000\,57$	2.02	6.31 ± 0.21	a	450	1.30 ± 0.17	5.52	9.83	2.64×1.5
J12121449−1422161	J1212−14	Type 1	0.1481 ± 0.0006	2.06	0.19 ± 0.01	a	600	1.33 ± 0.07	5.34	10.22	2.2×2
J13070062+2338052	J1307+23	Type 2	0.2741 ± 0.0012	3.31	0.41 ± 0.06	a	600	4.18 ± 2.43	5.54	10.63	2.2×1.5
J13213908+1342304	J1321+13	Type 2	$0.199 \pm 0.000\,32$	2.15	0.59 ± 0.02	a	600	1.15 ± 0.04	5.25	10.64	1.76×1.5
J13231468−0219013	J1323−02	Type 1	0.1606 ± 0.0003	2.25	7.82 ± 0.27	a	600	0.97 ± 0.15	5.33	10.66	2.2×1.5
J13384530−0438530	J1338−04	Type 1	$0.1625 \pm 0.000\,95$	1.99	12.6 ± 0.53	a	450	1.43 ± 0.49	5.57	10.98	2.2×1.5
J14073748+4256162	J1407+42	Type 2	$0.1183 \pm 9.9 \times 10^{-5}$	2.16	13.48 ± 0.59	a	600	1.24 ± 0.14	5.34	10.03	2.2×1.5
J14481932+4432324	J1448+44	Type 1	$0.0795 \pm 0.000\,31$	2.03	4.48 ± 0.08	a	300	1.12 ± 0.11	5.59	9.92	1.76×1.5
J16373652+2543028	J1637+25	Type 2	0.2769 ± 0.0001	2.33	0.16 ± 0.02	b	900	–	6.50	5.20	1.6×1.5
J21244163−1744458	J2124−17	Type 1	$0.1110 \pm 0.000\,55$	2.37	53.37 ± 1.58	b	300	–	6.50	6.00	2×1.5

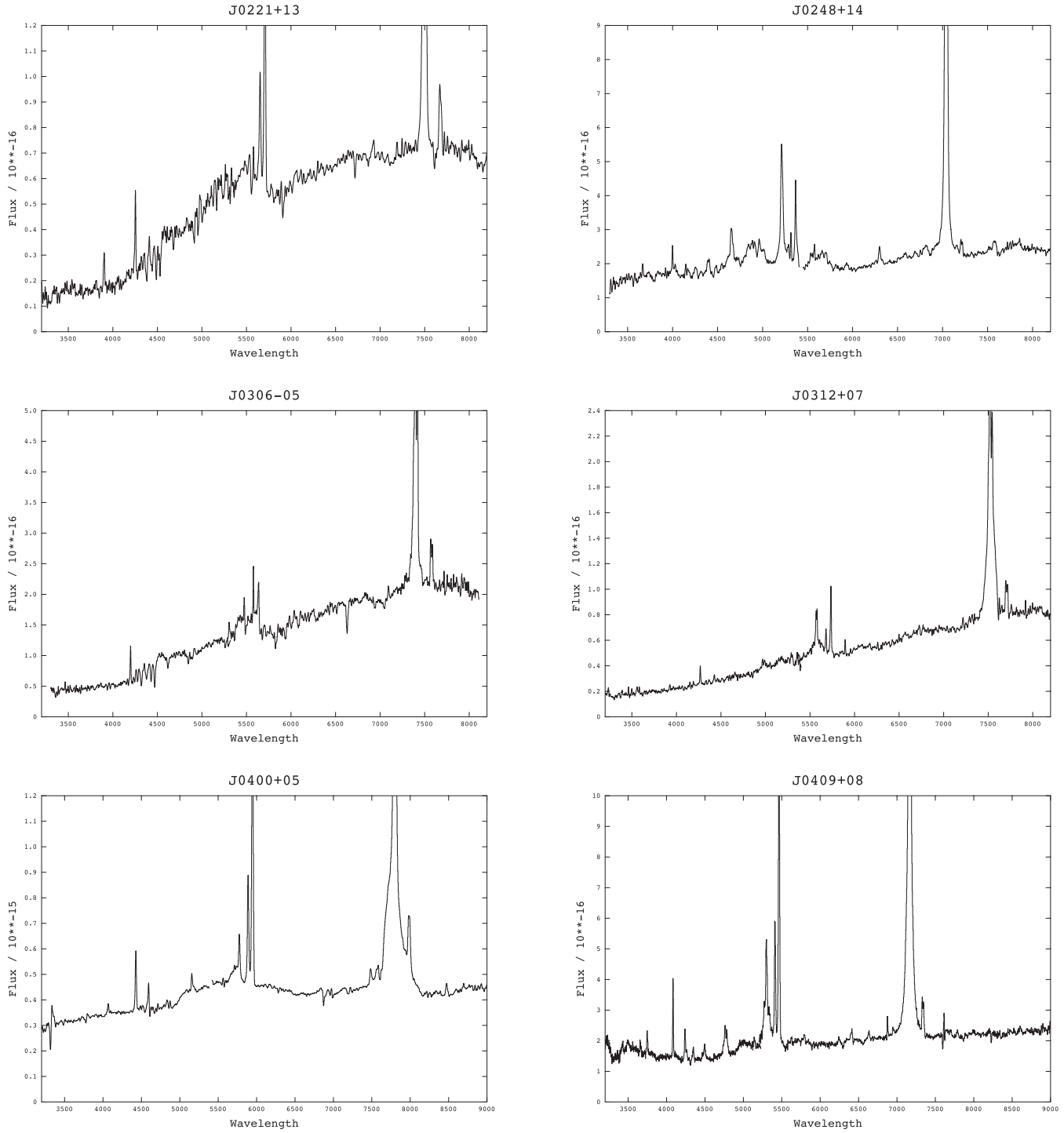

Figure 1. The combined (blue and red arm) spectra of the 2MASS sample discussed in this paper. Note the remarkable variety in the spectra: the spectral types range from type 2 Seyfert galaxies that lack the broad emission lines (e.g. J0504−19 and J1057−13), through highly reddened broad-line objects (e.g. J1040+59 and J1127+24), to objects that show optical spectra similar to 'normal' blue quasars (e.g. J1338−0438 and J2124−17), peculiar objects with strong FHILs in their spectra (e.g. J1131+16; Rose et al. 2011) and even LINER/H II region-like objects (e.g. J0411−01 and J1001+41). J1637+25 and J2124−17 have not had the telluric absorption features removed, because no telluric standard stars were observed during the particular run in which they were measured.

3 SAMPLES AND EMISSION-LINE FITTING

3.1 2MASS sample

The basic properties of the 2MASS sample are presented in Table 1. To give an indication of the intrinsic powers of the AGN, the [O III] emission-line luminosities ($L_{[O\,III]}$) were calculated using fluxes measured from the wide slit data for most objects; the narrow slit data were used where wide slit data were not available. For the purpose of calculating $L_{[O\,III]}$, the [O III] fluxes were corrected for Galactic reddening but not intrinsic reddening caused by dust in the host galaxies. $L_{[O\,III]}$ was chosen because the [O III]λ5007

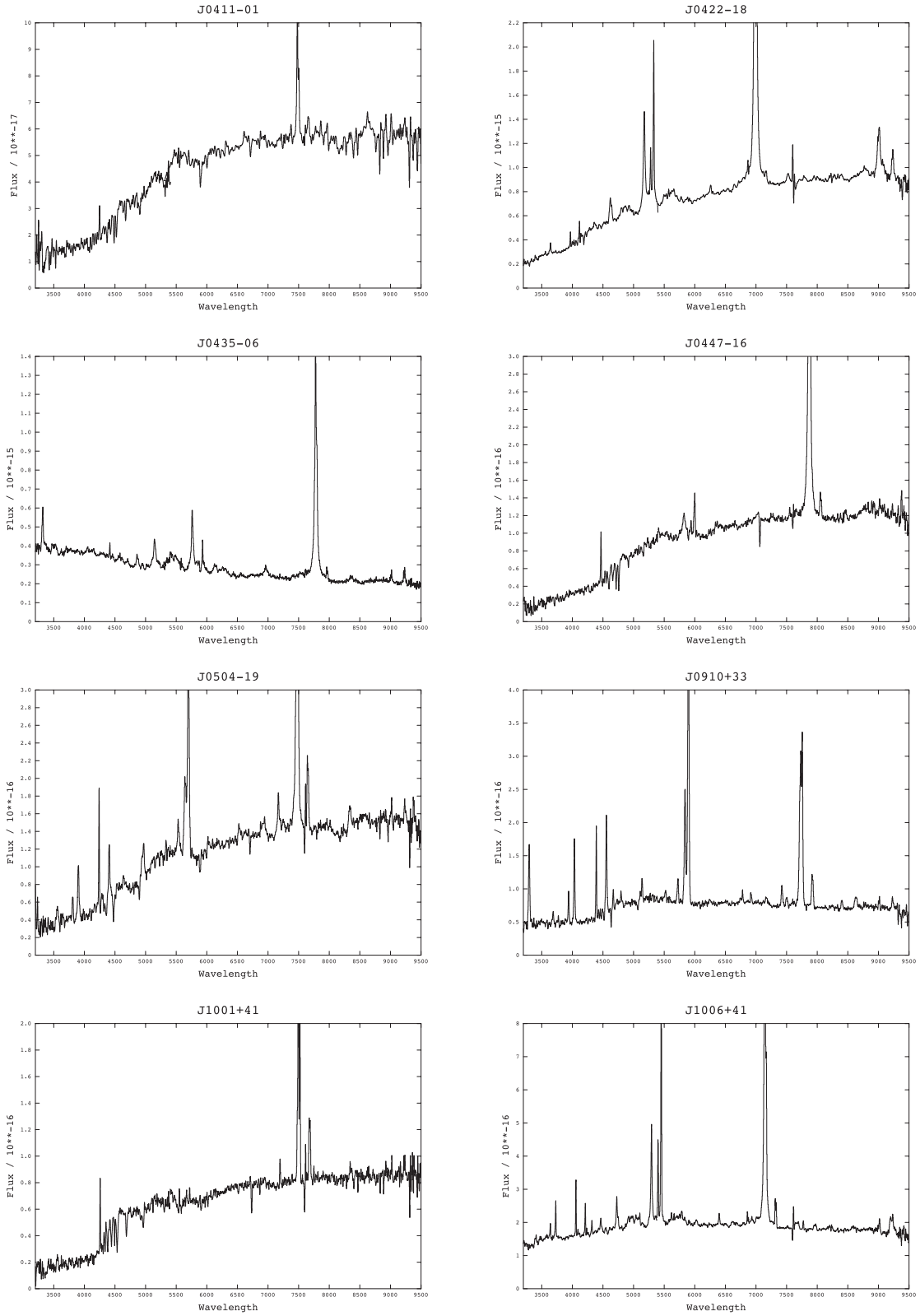

Figure 1 – *continued*

emission line is regarded as a good indicator of AGN bolometric power (Reyes et al. 2008; Dicken et al. 2009; LaMassa et al. 2010), and can be used to distinguish between quasars and Seyfert galaxies (Zakamska et al. 2003). The redshifts of the objects were determined by fitting single Gaussian profiles to the [O III]λ5007 emission lines.

The wide-to-narrow slit [O III] flux ratios are shown in Fig. 2. The majority of objects have wide and narrow slit fluxes that agree

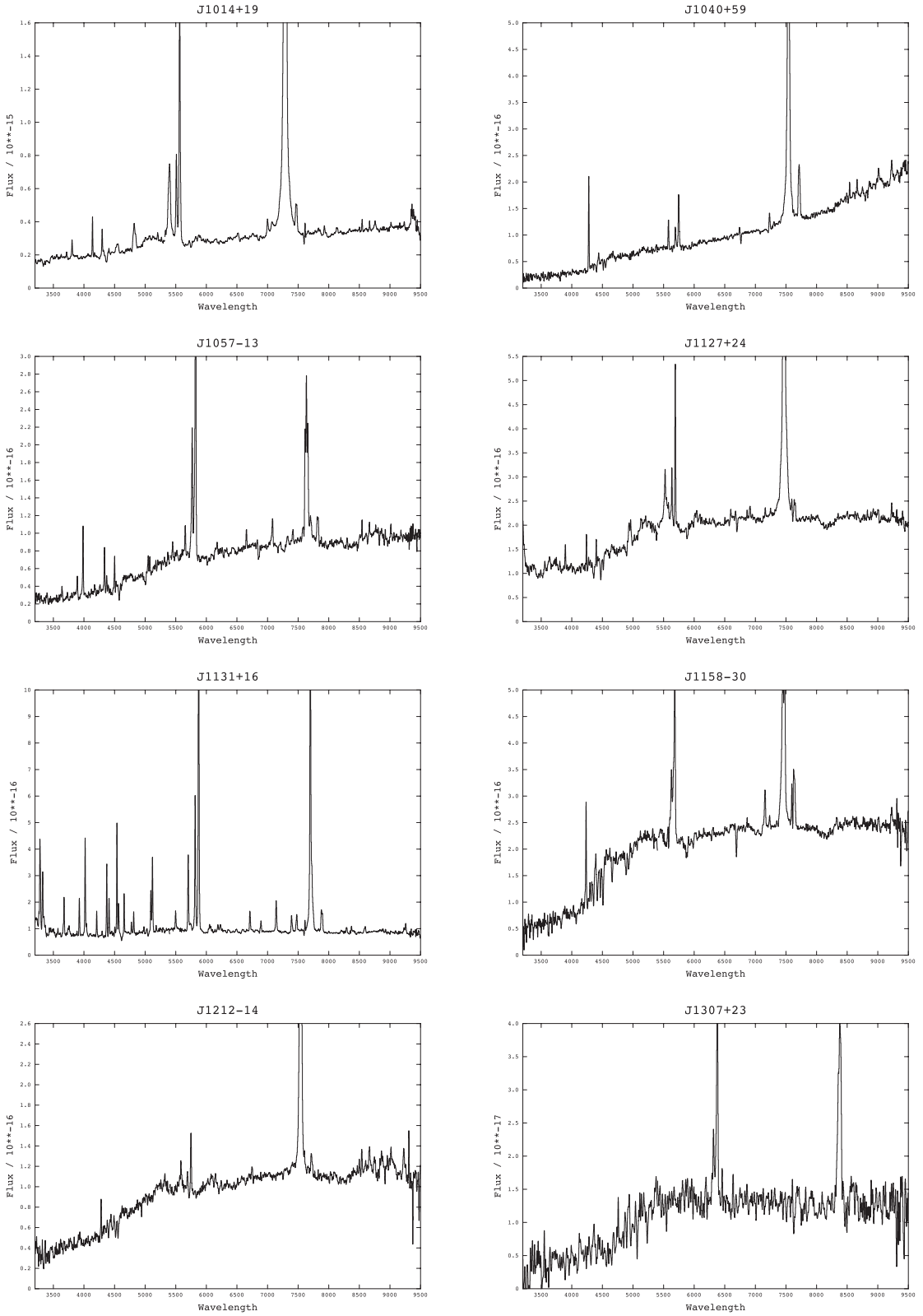

Figure 1 – *continued*

within ±40 per cent, suggesting that the narrower slits captured the majority of the flux from the emission regions: the median wide to narrow flux ratio is 1.14, showing that the wide slit captured slightly more flux than the narrow slit, as expected because the wide slit data probe a larger physical scale (4.9 to 22.7 kpc for the redshift range of this data) when compared to the narrow slit data (1.5 to 6.8 kpc). There are two outliers: J0435−06 and J1001+41, which have ratios above 1.5. However, the wide to narrow flux

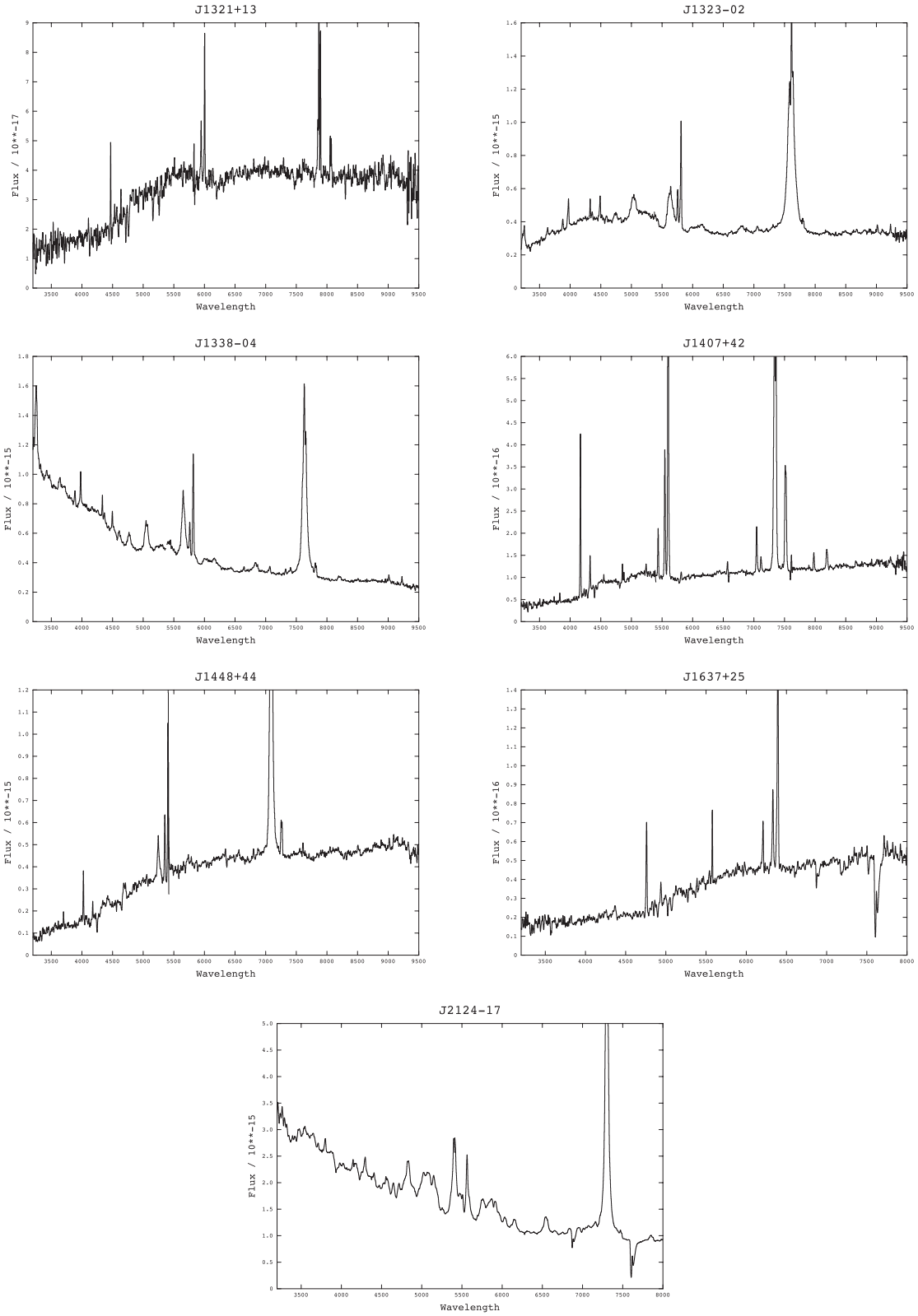

Figure 1 – *continued*

ratios for these objects agree within $\sim 2\sigma$ of the median ratio. In these cases, the [O III]λ5007 emission lines have a low equivalent width. Therefore, the large wide to narrow flux ratios in these objects may reflect the large uncertainties in [O III] fluxes, as measured from the noisy wide slit data, rather than uncertainties in the narrow slit fluxes. The similarity between the flux captured in the wide and narrow slit observations gives confidence that the spectra for the five objects without wide slit data (runs 'b' and 'c' in Table 1)

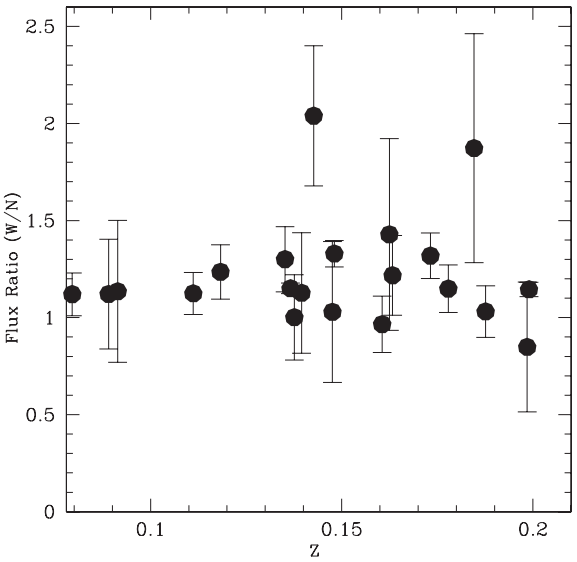

Figure 2. Wide to narrow [O III] flux ratio plotted against redshift for the 2MASS sample.

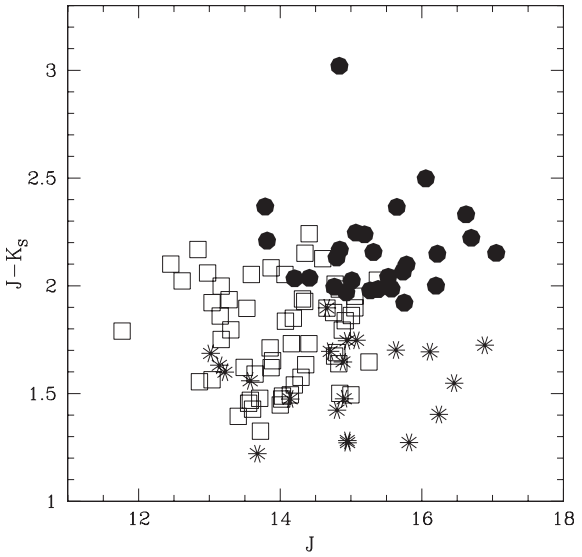

Figure 3. $J - K_S$ versus J for the 2MASS and comparison samples. The 2MASS population measurements are indicated by the filled circles, the PG quasar population (Boroson & Green 1992) are indicated by the unfilled squares and the unobscured type 1 AGN (Jin et al. 2012a; Jin, Ward & Done 2012b,c) are indicated by the asterisks. Higher values of $J - K_S$ indicate redder colours.

give an accurate indication (within ∼40 per cent) of $L_{[O\,III]}$ for these objects.

3.2 Comparison samples

In attempting to understand the nature of the red 2MASS AGN, some of the key questions we are trying to address are: if one takes a sample of AGN selected on the basis of their red colours at NIR wavelengths ($J - K > 2.0$), how do the optical spectroscopic properties of such a sample differ from those of samples of typical type 1 AGN selected using their optical/UV colours, and can any differences between the samples be explained in terms of reddening effects? Therefore, we have compared our results with two comparison samples of 'typical' quasars. For any comparisons we make, the samples we use are limited to redshifts $z < 0.2$, so they are consistent with our 2MASS AGN sample.

3.2.1 PG quasars

One of the comparison samples used throughout this paper is the PG quasar sample of Boroson & Green (1992). The PG quasars comprise a complete sample of 87 UV-selected objects from the Palomar bright quasar survey (Schmidt & Green 1983), selected to have redshifts $z < 0.5$, and UV/optical colours $U - B < -0.44$ to ensure an excess of flux in the UV. This sample is also selected to have quasar-like luminosities, with a total brightness of $M_B < -23$ for the AGN and host galaxy together, and broad permitted emission lines clearly present in the optical spectra (Boroson & Green 1992). The PG quasars provide a useful comparison with the 2MASS sample because they represent 'typical' blue selected quasars at their redshifts ($z < 0.5$). By limiting the redshift range of the sample, there are 61 PG quasars suitable for comparison with the red 2MASS sample. Spectra of the Boroson & Green (1992) sample were kindly supplied by T. Boroson, and remeasured by MR. The data cover a spectral range of λλ4300 to 5700 Å and have spectral resolutions in the range 6.5–7.0 Å. Detailed properties of the sample and the Fe II subtraction procedure are outlined in Boroson & Green (1992).

The spectra of the PG quasars were fitted in a similar manner to the 2MASS objects (see Section 3.3). However, in contrast to the 2MASS sample, only Hβ and [O III]λλ5007, 4959 were fitted for the PG quasars, due to the limited spectral range of their spectra (Boroson & Green 1992).

A subsample of these quasars (17) has high quality Sloan Digital Sky Survey (SDSS; York et al. 2000) spectra available, which cover a wider wavelength range than the spectra from the Boroson & Green (1992) study. We will refer to this as the PG/SDSS sample. Where possible, these spectra have been used as part of the comparison with the 2MASS sample.

As shown in Fig. 3, which plots the J magnitude against the $J - K_S$ colours, the PG quasars are comparatively 'bluer' than the 2MASS sample at NIR wavelengths (PG median: $J - K_S = 1.79 \pm 0.03$; 2MASS median: $J - K_S = 2.15 \pm 0.08$), with minimal overlap in $J - K_S$ colours between the samples: only 20 per cent of the PG sample has $J - K_S > 2.0$. In addition, the 2MASS objects are fainter in the J band. Given that the redshifts of the 2MASS objects in our sample are lower on average than those of the PG quasars, this suggests that the 2MASS objects have lower luminosities and therefore we may not be able to consider them as true quasars (see Section 4.1.1 for a full discussion).

3.2.2 Unobscured type 1 AGN

The second comparison sample comprises a sample of 51 relatively nearby ($z < 0.38$), unobscured type 1 AGN selected by Jin et al. (2012a,b,c) on the basis of low optical reddening, and low gas columns as indicated by their X-ray spectra. The optical properties of this sample were obtained from high quality SDSS data release 7 (DR7) spectra (Jin et al. 2012a,b,c). The SDSS DR7 spectra cover a wavelength range of 3800 to 9200 Å and have spectral resolution of ∼3 Å. The analysis techniques are outlined in the work of Jin et al. (2012a,b,c). There are 14 PG quasars in this sample, therefore, we have removed these from any comparison which includes the PG quasar sample to avoid overlap. In addition, when considering the remaining objects with redshifts $z < 0.2$, there are 21 unobscured type 1 AGN suitable for comparison. As these objects comprise

unobscured AGN, we consider this a suitable sample to compare to the red 2MASS quasars.

The spectral fitting technique outlined in Jin et al. (2012a) is similar to the methods we have used to fit the emission lines of our 2MASS sample (see Section 3.3). Therefore, we are confident that we can use the data presented in Jin et al. (2012a) for a direct comparison with our results.

As shown in Fig. 3, like the PG quasars, the unobscured type 1 AGN are also relatively 'blue' compared with the 2MASS sample at NIR wavelengths (median $J - K_S = 1.60 \pm 0.04$), with no overlap in $J - K_S$ colours between the samples. Unlike the PG quasars, this sample has comparable *J*-band magnitudes to the 2MASS sample. This suggests that, given the redshifts of the objects in the sample (median $z \sim 0.16$; for the entire sample), this sample has similar luminosities to the 2MASS objects.

3.3 Continuum subtraction and emission-line modelling

Fitting emission features in AGN spectra is often complicated by the presence of the host galaxy continuum in the spectrum. Subtle features such as weak broad components can often be overlooked, and the presence of underlying Balmer absorption from the stellar continuum can lead to an underestimation of the intensity of the Balmer and other emission-line strengths (e.g. Sarzi et al. 2006).

For the purposes of studying the emission regions, the underlying continuum was modelled and subtracted in all objects in which the stellar continuum is significant – mainly low-ionization nuclear emission-line region (LINER)/type 2 Seyfert objects (e.g. J0221+13) and objects with weak broad lines (e.g. J0422−18). These steps required the use of the Starlink package DIPSO (Howarth et al. 2004) and a customized IDL minimum χ^2 fitting program called CONFIT (Robinson et al. 2000; Tadhunter et al. 2005; Holt et al. 2007; Rodríguez Zaurín, Tadhunter & González Delgado 2009).

We started by experimenting with subtracting a nebular continuum component, which might be significant at near-UV wavelengths (Dickson et al. 1995). The contribution of the nebular continuum was estimated using the narrow Hβ emission-line flux. However, its strength is sensitive to the reddening of the narrow-line region (NLR), which is not accurately known in most cases. Indeed, we found that in all cases we obtained better fits if we did not subtract a nebular continuum. Therefore, the results below refer to models without nebular continuum subtraction.

Once the spectra had been prepared, the continua were modelled using the customized IDL procedure CONFIT (Robinson et al. 2000; Holt et al. 2007). To minimize degeneracy when fitting our spectra, we fit the smallest number of stellar and/or power-law components to the continuum as possible. For each object we ran three sets of models. In the first run, we fitted an unreddened old stellar population (OSP, 12.5 Gyr) and a young stellar population (YSP), with ages in the range 0.001–5 Gyr, and reddening: $0 < E(B - V) < 2.0$.[3] The inclusion of a YSP is justified on the basis that many of the objects with significant stellar continua show higher order Balmer lines in absorption (e.g. J1001+41). The stellar population templates were taken from the instantaneous burst spectral synthesis results of Bruzal & Charlot (2003) for a Salpeter initial mass function and solar metallicities. For the second run a power-law component, which represents either the direct or scattered AGN component, was also included in the model fitting. Finally, an OSP with and without a power law was fitted to each spectrum, independent of a YSP.

The spectra were fitted using fluxes measured in 30 Å bins, chosen to have as even a distribution in wavelength as possible, and avoiding the brighter atmospheric emission and stronger atmospheric absorption, and AGN emission, features in the spectra. The entire useful wavelength ranges of the spectra were fitted: observed wavelengths 3200–9000 Å. In addition, a normalizing bin was chosen which is also free of any emission/absorption features (∼5050–5200 Å for all objects in the rest frame).

Fits to the overall continuum shape were chosen with low reduced $\chi^2 < 1$ (see discussion in Tadhunter et al. 2005). Then a visual inspection of fits to individual absorption lines, including Ca II K (3934 Å), Mg I (5175 Å), Balmer and Na I D (5890–5896 Å), was used to select the best overall fits. Note that not all objects were successfully fitted. For example, we could not produce an adequate fit to the type 2 object J1131+16 because there are relatively few genuine continuum bins suitable to model the spectrum of this object. It should be noted that this object has an unusual spectrum, which contains a large number of forbidden high-ionization lines (FHILs; see Rose et al. 2011). Fig. 4 shows an example of a successful CONFIT fit to a 2MASS object. Details of the models chosen for the continuum subtraction in individual objects are given in Table 2.

Once the continuum had been subtracted from the spectra (where applicable), the emission lines were fitted using the Starlink DIPSO package (Howarth et al. 2004).

The emission lines in the spectra of the 2MASS and PG comparison sample AGN were initially fitted with single Gaussian profiles, starting with [O III]λλ5007, 4959 doublet. We used the [O III]λλ5007, 4959 emission lines because they are often the strongest unblended lines emitted by the NLR. To produce the models, Gaussian profiles were fitted to the [O III] doublet, with the separation and intensity ratio set by atomic physics for each kinematic component (as defined by the velocity shifts and line widths). While single Gaussian fits were sufficient in some objects, such fits did not adequately model the wings of the emission lines of most of the objects; in such objects double Gaussian model were fitted to the spectral lines. When a second Gaussian was added, the line ratios, wavelength separations and full width at half-maximum (FWHM) were fixed for the two doublet components as before, however, the shift and FWHM were allowed to vary relative to the first component. In all cases, one or two Gaussian components proved sufficient, and in all cases where two Gaussian profiles were required, the width of one Gaussian was significantly broader than the other. In some cases, the widths of the narrow components for the [O III] emission lines were found to be consistent with the instrumental width of their spectra. In such cases, the narrow components of the models that were fitted to the other lines were fixed to the instrumental width. However, in the other (resolved) cases, the measured FWHM was used to obtain an intrinsic velocity width for the narrow component by correcting its FWHM in quadrature using the instrumental width. The same technique was applied to the broader components of the model. Also, the broad component is often shifted with respect to the narrow component; this is accounted for in the models.

Once the model parameters had been determined from the fits to [O III], they were used to fit the other lines in the spectra. The [O III] model parameters for each object are presented in Table 3. Known blends (e.g. Hα and [N II]λλ6548, 6583) and doublets (e.g. [S II]λλ6716, 6731 and [O II]λλ3726, 3729) were modelled with the [O III] model using constraints provided by atomic physics (i.e. fixed FWHM, line separation and, where appropriate, the intensity ratios set by atomic physics). In most cases, the [O III] model successfully

[3] We used the Calzetti et al. (2000) reddening law to redden the YSP spectra.

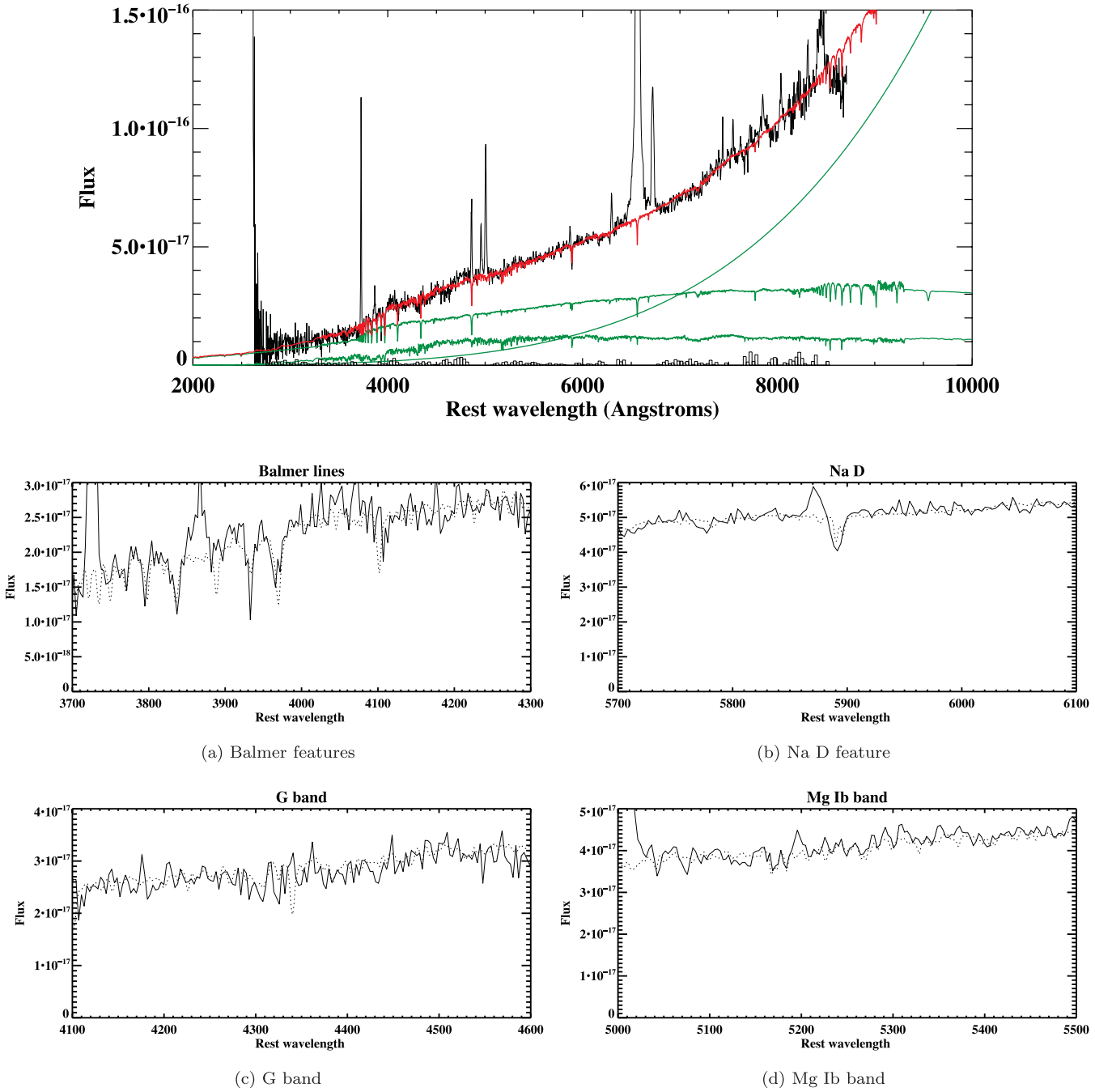

(a) Balmer features

(b) Na D feature

(c) G band

(d) Mg Ib band

Figure 4. A best-fitting CONFIT model for J10404364+5934092 ($\chi^2 = 0.54$), plots (a)–(d) show how the combined stellar populations fit the detailed features. The object requires an OSP, a YSP and a power-law component for an adequate fit. The YSP has an age of 0.005 Gyr, an extinction of $E(B-V) = 1.0$ and represents 58.7 per cent of the flux in the normalizing bin. The power-law component has $\alpha = 5.11$ and represents 16.4 per cent of the flux in the normalizing bin. Finally, the OSP represents 24.8 per cent of the flux in the normalizing bin. The flux is in units of erg s^{-1} cm^{-2} Å^{-1} and wavelength is in units of Å.

fit all the emission lines/blends in the spectra. However, in a few cases where emission lines have a low equivalent width (e.g. weaker lines such as [O I] or [FeX]), one of the components in the two component [O III] model provides a better fit to the emission line. This happened in some objects with strong broad Balmer emission lines.

The broad permitted lines emitted by many of the objects (mainly Hα and Hβ) were initially fitted with a single Gaussian component, where the intrinsic velocity widths (FWHM) were kept the same for the all broad-line region (BLR) emission lines in each object. The NLR emission components of the Balmer emission were still fitted with the [O III] model. However, for 11 objects in the 2MASS sample, the broad- and narrow-line components of the Balmer lines could not be confidently separated because, at the resolution of our spectra, they merge seamlessly together, leading to degeneracies in fits that attempt to model the lines as single narrow and broad Gaussians (see Fig. 5). In addition, for the PG/SDSS sample, we could only confidently separate the broad and narrow emission in six objects. Fig. 5 highlights the problem of degeneracy in the blending of the NLR with BLR in the Balmer lines, using the example of

Table 2. Best-fitting CONFIT model results for the 2MASS sample. The simple stellar population models were taken from Bruzal & Charlot (2003). The subscripts 'U' and 'L' refer to the upper and lower cases of the model parameters that provide a good fit to the continuum. For the cases where the best fits include power laws we use the form $F_\nu \propto \nu^{+\alpha}$, where α represents the power-law index.

Object	YSP_U (Gyr)	YSP_L (Gyr)	$E(B-V)_U$	$E(B-V)_L$	α_U	α_L
J0221+13	1.0	0.7	0.5	0.3	2.18	0.457
J0306−05	2.0	0.8	0.5	0.3	3.95	1.40
J0411−01	0.006	0.005	1.1	0.6	–	–
J0422−18	0.005	0.004	1.1	0.9	2.35	0.32
J0447−16	1.2	0.8	0.3	0.2	1.31	1.28
J0504−19	0.01	0.006	0.9	0.7	–	–
J0910+33	0.9	0.3	0.3	0.1	−0.347	−0.818
J1001+41	0.2	0.1	0.7	0.6	–	–
J1040+59	0.005	0.004	1.1	0.8	5.97	5.11
J1057−13	2.0	0.2	0.6	0.0	−0.30	−1.33
J1158−30	0.4	0.2	0.5	0.2	2.86	1.74
J1212−14	1.2	0.8	0.4	0.2	1.07	0.627
J1321+13	0.05	0.005	0.7	0.4	–	–
J1407+42	0.06	0.04	0.6	0.5	–	–

Table 3. The [O III] model parameters used when fitting the emission lines of the spectra. The second and third columns present the rest-frame widths of the narrow and broad kinematic components, respectively. The final column gives the rest-frame velocity separation of the broad relative to the narrow kinematic components. Note that the line widths have been corrected for the instrumental width.

Object	$FWHM_N$ (km s^{-1})	$FWHM_B$ (km s^{-1})	Separation (km s^{-1})
J0221+13	Inst.	799 ± 36	−217 ± 27
J0248+14	448 ± 39	945 ± 61	−168 ± 44
J0306−05	Inst.	826 ± 148	−426 ± 152
J0312+07	Inst.	718 ± 95	−227 ± 72
J0400+05	326 ± 13	1197 ± 51	−36 ± 11
J0409+07	620 ± 22	1842 ± 340	−44 ± 68
J0411−011[a]	544 ± 150	–	–
J0422−18[b]	Inst.	1700 ± 56	−298 ± 31
J0435−06	256 ± 19	376 ± 84	−655 ± 93
J0447−16	194 ± 7	1072 ± 165	−569 ± 187
J0504−19[b]	Inst.	1778 ± 40	191 ± 32
J0910+33	715 ± 21	1652 ± 48	−276 ± 33
J1001+41[a]	418 ± 76	–	–
J1006+41[b]	Inst.	554 ± 159	−353 ± 152
J1014+19	428 ± 13	1637 ± 63	127 ± 23
J1040+59	181 ± 22	993 ± 84	214 ± 62
J1057−13	707 ± 14	1477 ± 139	−855 ± 116
J1127+24	267 ± 7	–	–
J1131+16[c]	Inst.	720 ± 31	−92 ± 5
J1158−30	693 ± 27	1177 ± 139	−1195 ± 66
J1212−14[a]	455 ± 25	–	–
J1321+13[a]	390 ± 14	–	–
J1323−02	366 ± 16	1512 ± 108	−488 ± 94
J1338−04[b]	Inst.	780 ± 24	−224 ± 34
J1407+42	584 ± 8	1316 ± 48	190 ± 28
J1448+44[a]	441 ± 15	–	–
J2124−17[a]	753 ± 22	–	–

[a]The model for this object requires just one component.
[b]The narrow component of the model can be modelled with the instrumental width.
[c]This object was studied in detail in Rose et al. (2011).

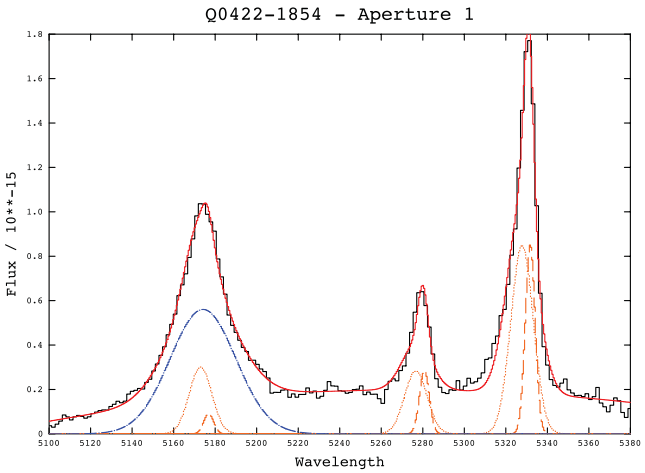

Figure 5. Gaussian fits to the Hβ and [O III]$\lambda\lambda$5007, 4959 emission lines of J0422−18. The overall fit is represented by a red line. Both the NLR [O III] model (orange lines; the narrow component is represented by a dashed line and the broad component is presented by a dotted line) and BLR components (represented by a blue dashed and dotted line) are displayed. The NLR model fit to the Hβ blend highlights the degeneracy issues with blended emission from the BLR and the NLR (this is described in more detail in Section 3.3).

J0422−18. Although the overall fit to the Hβ feature is adequate, the narrow-line Gaussian fitted to the Hβ emission line may be over- or underestimating the flux of the NLR Hβ emission. In such cases, we only consider the total fluxes of the combined broad and narrow emission components of the Balmer lines.

The Hβ and [O III]$\lambda\lambda$5007, 4959 may also be strongly blended with broad permitted Fe II emission. In cases where broad permitted Fe II emission is prominent in the spectra (e.g. J0248+14), the Fe II emission was fitted separately from the affected emission lines as follows: the Fe II emission lines in the same multiplets (F, S or G) were fitted with the same intrinsic velocity widths as the broad Hβ emission line, and their expected intensity ratios were used to constrain the fits, as outlined in Kovačević, Popović & Dimitrijević (2010). This approach provided a good fit to the Fe II emission blends in all objects where they are significant.

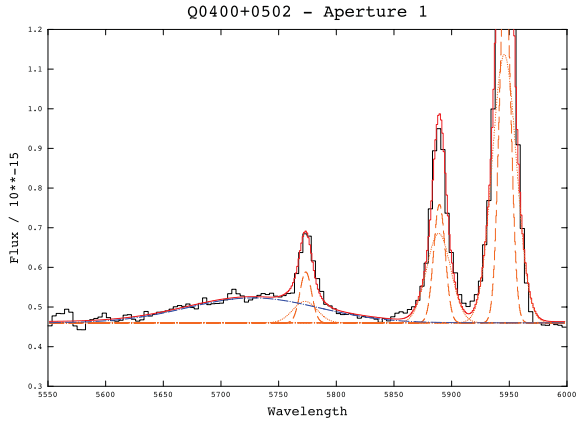

Figure 6. Gaussian fits to the Hβ and [O III]$\lambda\lambda$5007, 4959 emission lines of J0400+05. Both the NLR [O III] model and BLR components are displayed. In this case the BLR and NLR components of Hβ could be clearly separated. Interestingly, the BLR is substantially blueshifted relative to the NLR in this object (by -2870 ± 160 km s^{-1}). The properties of the individual objects in the 2MASS sample with particularly interesting spectra are discussed in the Appendix.

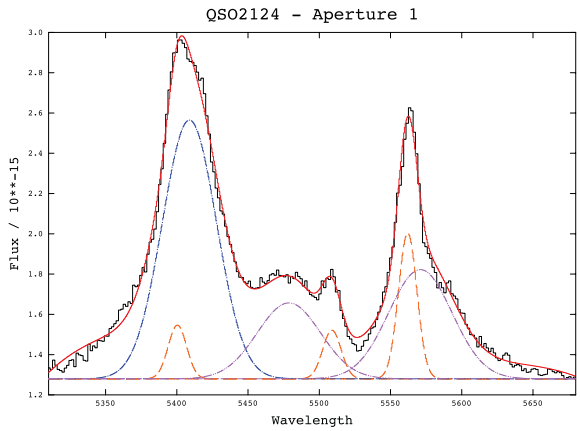

Figure 7. Gaussian fits to the Hβ and [O III]$\lambda\lambda$5007, 4959 emission lines of J2121−17. The NLR [O III] model, BLR component and Fe II emission (represented by a violet dashed and dotted line) are displayed. The overall fit is far better than when the emission lines are modelled without the Fe II emission.

Examples of model fits are given in Figs 6 and 7. Fig. 6 shows an example of a multicomponent Gaussian fit to Hβ and [O III]$\lambda\lambda$5007, 4959, where the broad and narrow components of Hβ were easy to separate. Interestingly, the BLR of this object is substantially blueshifted relative to the NLR in this object (by -2870 ± 160 km s^{-1}). Fig. 7 shows a case where the broad and narrow emission could not be easily separated, and where Fe II emission is prominent. The properties of the individual objects in the 2MASS sample with particularly interesting spectra are discussed in the Appendix.

The results for the NLR [O III] model fits to the other lines are presented in Table 4; all the emission-line ratios are presented relative to [O III]λ5007, and the NLR and BLR Balmer components are presented separately.

4 RESULTS

The optical spectra of the 2MASS sample, shown in Fig. 1, reveal a remarkable variety, ranging from type 2 Seyfert galaxies that lack broad emission lines (e.g. J0504−19 and J1057−13), through highly reddened broad-line objects (e.g. J1040+59 and J1127+24), to objects that show optical spectra similar to 'normal' blue quasars (e.g. J1338−04 and J2124−17) and even LINER/H II region-like objects (e.g. J0411−01 and J1001+41). We now describe the results obtained from the detailed analysis of the spectra.

4.1 Quasars, AGN or starbursts?

4.1.1 Quasars?

Previous studies of red 2MASS AGN have shown that most red 2MASS AGN in the local Universe are not quasars, but have luminosities more consistent with those of Seyfert galaxies (Smith et al. 2002; Marble et al. 2003; Kuraszkiewicz et al. 2009a,b).

To test the incidence of quasars in our low-z 2MASS sample, we used the [O III]λ5007 emission-line luminosity, which has been shown to be a good indicator of AGN bolometric power (see Heckman et al. 2004; Bian et al. 2006; Dicken et al. 2009; LaMassa et al. 2010). Other luminosity indicators, such as the L_{5100} optical continuum luminosity, cannot be accurately calculated in most of the 2MASS objects because of a combination of reddening of the AGN continuum and host galaxy contamination. Following Zakamska et al. (2003), we assume that an object is a quasar if it has an [O III]λ5007 luminosity $L_{[\mathrm{O\,III}]} \gtrsim 10^{35}$ W, corresponding to a nuclear continuum luminosity of $M_B \lesssim -23$ (Schmidt & Green 1983; Zakamska et al. 2003).

Fig. 8 shows $L_{[\mathrm{O\,III}]}$ plotted against redshift for the 2MASS objects and the comparison samples. Note that the luminosities have been determined using the observed frame [O III]λ5007 fluxes and the luminosity distances appropriate for the assumed cosmology, but have not been corrected for intrinsic reddening. Where possible we use the wide slit (5 arcsec) data to ensure that the AGN [O III] luminosity measurements are not affected by slit losses; for the five objects for which there are no wide slit data, we use the available 1.5 arcsec data. We find that five objects in our sample (19 per cent) qualify as quasars according to the [O III] emission-line luminosity criterion: J0400+05, J1131+16, J1338−04, J1407+42 and J2124−17. Note that the latter object was previously identified as an ultraluminous infrared galaxy (ULIRG) by Kim & Sanders (1998).

The rate of quasars for the 2MASS sample (filled circles) is comparable to that of the rate of quasars in the comparison samples ($z < 0.2$): 28 per cent of the PG quasars (unfilled squares) and 10 per cent of the unobscured type 1 AGN (asterisks) have quasar-like luminosities based on the $L_{[\mathrm{O\,III}]}$ luminosity. Therefore, the rate of occurrence of quasars in the PG and unobscured type 1 samples is not significantly different from that of the 2MASS sample. However, we note that four objects in our 2MASS sample have lower [O III] emission-line luminosities than any of the objects in the PG quasar and unobscured type 1 AGN samples.

We can only be confident that five of the objects in the sample are genuine quasars. The remaining sample has [O III] luminosities in the range $32.5 < \log_{10}(L_{[\mathrm{O\,III}]}) < 35$ W – more typical of Seyfert galaxies. If the four objects with low [O III] luminosities are ignored, then the 2MASS AGN will have a similar range of luminosities as the PG quasars and the unobscured type 1 AGN. Note that we have not corrected the [O III] emission-line luminosities for intrinsic dust extinction. If we correct the emission-line luminosities using the NLR reddening estimates available for 16 objects (Section 4.2.1), we find that the rate of occurrence of quasars in the 2MASS sample increases to 27 per cent (eight objects). However, we emphasize that

Table 4. Emission-line fluxes of the key emission lines in the 2MASS sample, given as a ratio to the flux of the [O III]λ5007 emission line (in units of erg s^{-1} cm^{-2}, presented in column 2). The BLR and NLR emission is indicated separately for the Hα and Hβ emission lines. In general, the uncertainties associated with the emission-line fluxes do not exceed ± 10 per cent.

Object	$F_{[O\,III]}$	[Ne V] 3425	[O II] 3727	[Ne III] 3868	Hδ	Hγ	[O III] 4363	$H\beta_{NLR}$	$H\beta_{BLR}$	[FeV II] 6086	[O I] 6300	[FeX] 6374	$H\alpha_{NLR}$	$H\alpha_{BLR}$	[N II] 6583	[S II] 6716 and 6731
0221+13	1.8E−15	0.226	0.264	3.971	–	–	–	0.203	–	0.128	0.030	–	0.610	–	1.139	0.420
0248+14	2.0E−15	0.208	0.446	0.323	0.495	0.789	0.179	2.190	1.052	–	0.106	–	17.841	5.535	4.395	0.476
0306−05	2.1E−15	–	0.285	–	–	–	–	0.761	–	–	0.163	–	6.751	–	3.578	0.950
0312+07	7.6E−16	0.023	0.065	0.024	–	0.111	–	0.818	2.721	0.038	0.082	–	3.586	14.832	1.442	1.041
0400+05	3.0E−14	0.027	0.151	0.059	0.013	0.046	–	0.095	0.391	–	0.025	0.061	0.668	3.157	0.420	0.259
0409+08	2.1E−14	0.052	0.125	0.070	0.009	0.026	0.015	0.185	0.675	0.024	0.031	0.017	0.926	1.124	0.173	0.138
0411−01	1.5E−16	–	1.044	–	–	0.487	–	1.639	–	–	0.139	–	7.031	–	3.224	1.578
0422−18	2.8E−14	0.049	0.056	0.075	0.070	0.181	0.108	0.854	0.522	–	0.010	–	0.464	5.357	0.916	0.069
0435−06	2.3E−15	–	0.338	–	0.362	1.059	–	2.420	3.752	–	0.035	–	12.498	8.809	0.970	0.496
0447−16	1.2E−15	–	0.504	–	–	–	–	0.169	1.224	0.072	0.150	–	0.508	11.667	3.362	0.544
0504−19	8.4E−15	0.166	0.191	0.219	–	0.088	0.105	0.179	–	–	0.038	–	0.686	–	0.736	0.275
0910+33	1.3E−14	0.132	0.112	0.173	0.022	0.030	0.036	0.098	–	0.022	0.040	0.016	0.211	–	0.367	0.121
1001+41	2.4E−16	–	2.532	4.897	–	0.812	0.128	2.102	–	–	1.204	–	16.816	–	9.636	5.907
1006+41[a]	1.2E−14	0.114	0.158	0.266	0.045	0.161	0.055	0.520	–	–	0.037	0.014	1.707	1.393	0.315	0.171
1014+19	3.6E−14	0.045	0.076	–	0.011	0.020	0.047	0.385	0.517	0.008	0.035	0.046	2.141	2.881	0.303	0.128
1040+59[a]	2.1E−15	–	1.073	0.157	–	0.083	–	0.516	–	–	0.248	–	1.118	5.143	0.434	1.573
1057−13	8.9E−15	0.123	0.078	0.071	0.021	0.035	0.014	0.052	–	0.081	0.055	–	0.368	–	0.105	0.105
1127+24	5.1E−15	0.084	0.147	0.132	0.057	0.094	–	0.264	0.909	0.079	0.077	–	0.857	4.886	0.376	0.203
1131+16	2.3E−14	0.192	0.138	0.209	0.046	0.083	0.171	0.190	–	0.094	0.037	0.044	0.948	–	0.149	0.103
1158−30	9.2E−15	–	0.345	0.118	–	0.106	–	0.121	–	–	0.162	–	1.328	–	0.658	0.365
1212−14	4.5E−15	0.104	0.415	–	–	–	–	0.325	1.182	–	0.005	–	1.646	5.565	1.593	0.507
1307+23	9.4E−16	–	0.045	–	–	0.121	0.019	0.084	–	–	0.011	–	0.254	–	0.283	0.048
1321+13	6.8E−16	0.089	0.417	0.156	–	–	–	0.254	–	–	0.105	–	1.444	–	0.900	0.491
1323−02	1.4E−14	0.173	0.082	0.130	–	0.011	0.021	0.049	1.827	0.074	0.025	–	1.264	7.657	1.980	0.132
1338−04	1.4E−14	0.233	0.140	0.124	0.011	0.015	0.042	0.092	1.461	0.080	0.074	0.045	0.426	5.397	0.222	0.108
1407+42	1.6E−14	0.014	0.319	0.069	0.032	0.063	0.010	0.139	–	0.029	0.124	–	0.947	–	0.685	0.481
1448+44	1.4E−14	0.046	0.203	0.077	–	–	–	0.074	0.722	–	0.046	–	0.473	3.422	0.461	0.260
1637+25	2.3E−15	0.042	0.371	0.087	0.030	0.054	0.125	0.264	–	–	–	–	–	–	–	–
2121−17	2.7E−14	0.113	0.112	–	–	0.434	0.913	0.498	2.685	–	0.089	–	5.152	1.680	3.141	0.083

[a]Only Hα was detected for the BLR of this object.

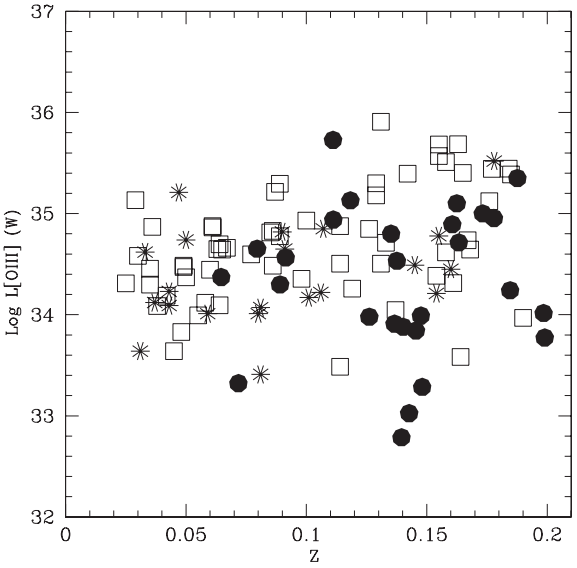

Figure 8. [O III] emission-line luminosity ($L_{[O\,III]}$) plotted against redshift for the 2MASS objects and the comparison samples. The 2MASS objects are represented by the filled circles, the PG quasars are represented by the unfilled squares and the unobscured type 1 AGN are represented by the asterisks. Objects with $L_{[O\,III]}$ greater than 10^{35} W are likely to have quasar-like bolometric luminosities.

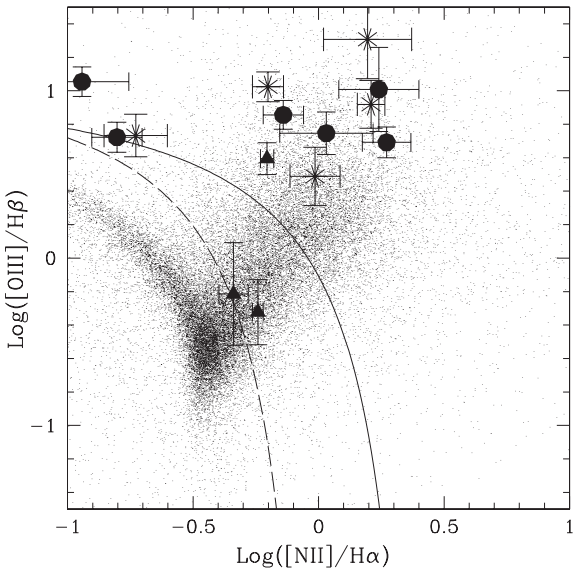

Figure 9. Diagnostic plot of $\log_{10}([O\,III]/H\beta)$ versus $\log_{10}([N\,II]/H\alpha)$. AGN are defined to lie above the solid line, H II region-like galaxies below the dashed line and composite galaxies between these boundaries. The filled circles indicate the emission-line measurements for type 2 objects in the 2MASS sample, the stars represent narrow-line emission from the type 1–1.9 objects, the triangles represent the objects in the 2MASS sample, which have fainter emission than the rest of the sample, and the small points are from SDSS DR8 data.

we can only accurately correct the narrow-line fluxes for reddening in 55 per cent of the objects.

4.1.2 AGN or starbursts?

Both starburst and AGN activity can potentially ionize the narrow emission regions in the nuclei of galaxies (Baldwin, Phillips & Terlevich 1981). It is therefore important to establish whether the NLR in the 2MASS objects are indeed photoionized by AGN, or whether recent starburst activity provides the photons needed to ionize the emission-line regions. Therefore, we have categorized the spectra based on the emission-line ratios using Baldwin, Phillips & Terlevich (BPT) diagnostic diagrams (e.g. see Baldwin et al. 1981; Kewley et al. 2006).

Figs 9–11 show the results for the 2MASS sample. The divisions between the different classes of objects in these figures are taken from Kewley et al. (2006). Note that only ∼50 per cent of the 2MASS sample could be plotted on the BPT diagrams because of the difficulty of measuring accurate narrow Hβ emission-line fluxes in many of the objects, related to the deblending of the emission of the BLR and the NLR (see discussion in Section 3.3).

Based on the diagnostic diagrams, all of the objects that could be plotted fall in the AGN part of the diagrams with the exceptions of J0411−01 and J1001+41, which fall in the composite/H II region of the diagrams, suggesting a major contribution from stellar photoionization.

In addition to emission-line diagnostic ratios plotted in Figs 9–11, the presence of FHILs in the spectra can indicate unambiguously the presence of an AGN. These lines include [Ne V]λλ3345, 3426, [Fe VII]λ6086 and [FeX]λ6374 which, due to their high ionization potentials (>97 eV), are not generally associated with LINER nuclei or starbursts. We find that 23 of the objects in our sample (85 per cent) show evidence for at least one FHIL, suggesting significant AGN activity.

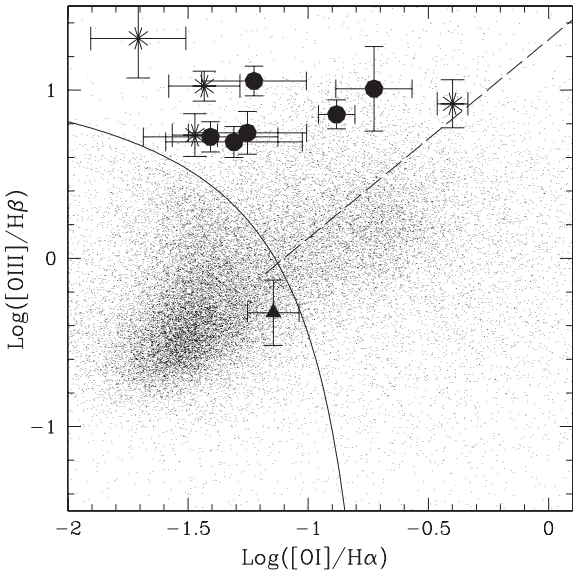

Figure 10. Diagnostic plot of $\log_{10}([O\,III]/H\beta)$ versus $\log_{10}([O\,I]/H\alpha)$. AGN are defined to lie above the solid line, with the dashed line separating Seyfert-type objects (above the line) and LINER-type objects (below). H II region-like galaxies fall below the solid line. The symbols are the same as Fig. 9.

Another indicator of the presence of an AGN is the detection of broad-line emission from the BLR. Table 5 indicates whether broad emission lines are detected for each of the 2MASS objects. We assume that the BLR is detected if the Balmer recombination lines show significant (i.e. well above the noise) broad wings that cannot be accounted for by the [O III] model, and have FWHM > 1000 km s^{-1}. 16 out of 27 objects in our sample (59 per cent) show

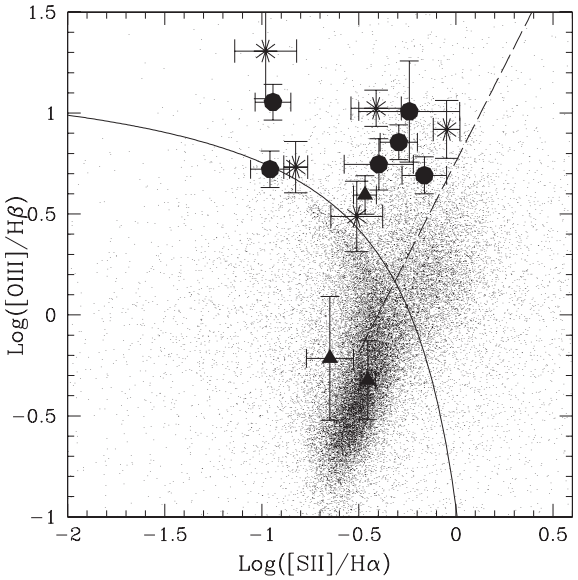

Figure 11. Diagnostic plot of $\log_{10}([\mathrm{O\,III}]/\mathrm{H}\beta)$ versus $\log_{10}([\mathrm{S\,II}]/\mathrm{H}\alpha)$. AGN are defined to lie above the solid line, with the dashed line separating Seyfert-type objects (above the line) and LINER-type objects (below). H II region-like galaxies fall below the solid line. The symbols are the same as in Fig. 9.

the presence of definite BLR emission. In addition, tentative evidence for weak Hα broad-line emission in J1131+16 was presented in Rose et al. (2011). The broad-line component in J1131+16 is consistent with the presence of a scattered (Antonucci & Miller 1985), or a directly observed, but weak, BLR component. The rest of the type 2 objects had no such emission.

Fig. 12 presents the velocity widths (FWHM) of the BLR components as measured from single Gaussian fits to the broad Balmer lines,[4] plotted against $L_{[\mathrm{O\,III}]}$ for both the 2MASS sample and PG sample. Where possible, the broad- and narrow-lines emission were fitted separately in order to obtain the BLR FWHM; such cases are indicated by the filled circles. Where the broad and narrow components could not be confidently separated we use the velocity widths of single Gaussian fits to the whole profiles; these cases are indicated by the black triangles. The median BLR velocity width (FWHM) for the 2MASS sample is 2100 ± 400 km s^{-1}, which is lower than that of the PG sample (4500 ± 300 km s^{-1}). However, the 2MASS median may be affected by the inclusion of NLR emission in the objects for which we could not confidently separate the emission from the BLR and the NLR. The median velocity width for the 2MASS objects in which the broad and narrow components could be confidently separated is 4400 ± 1100 km s^{-1} – comparable with the PG quasars.

All the results from this section are summarized in Table 5. Overall, 25/27 (∼93 per cent) of the objects show some sign of AGN activity; and only two objects – J0411−01 and J1001+41 – show no clear evidence of AGN activity. Given that it is not clear whether the latter two objects are powered by AGN activity, we do not include them in the analysis in the rest of the paper. In terms of a more detailed classification of the spectra of the 2MASS objects for which we detect significant AGN activity, 59 per cent qualify as type 1 Seyfert galaxies, 30 per cent as type 2 Seyfert galaxies, and 11 per cent have weak broad lines placing them between the type 1 and 2 Seyfert classification.

[4] Note that the FWHM of the Balmer lines is based on fits to the Hβ in all cases except for J1006+41 and J1040+59, which do not have any detectable broad emission in the Hβ emission line, but clear BLR Hα components.

Table 5. Truth table presenting the evidence for AGN activity in the 2MASS sample objects. A true result for BLR indicates the detection of a broad component for either/both Hα and Hβ. A true result for the FHIL indicates the positive detection of a high ionization species (>54.4 eV). The [N II] column shows the results from Fig. 9, the [O I] column shows Fig. 10 and the [S II] column shows Fig. 11. T = true, F = false, P = tentative evidence for a BLR, A = AGN, S = Seyfert type, H = starburst galaxy, C = composite galaxy, D = unmeasured due to the degeneracy between the broad and narrow Balmer emission, and X = unmeasured because an appropriate emission line has not been detected.

Name	Quasar	BLR	FHIL	[N II]	[O I]	[S II]
0221+13	F	F	T	A	S	S
0248+14	F	T	T	D	D	D
0306−05	F	F	T	D	D	D
0312+07	F	T	T	D	D	D
0400+05	T	T	T	A	S	S
0409+08	F	T	T	A	S	S
0411−01	F	F	F	C	X	H
0422−18	F	T	T	D	D	D
0435−06	F	T	F	D	D	D
0447−16	F	T	T	D	D	D
0504−19	F	F	T	A	S	S
0910+33	F	F	T	A	S	S
1001+41	F	F	F	C	H	H
1006+41	F	T	T	D	D	D
1014+19	F	T	T	D	D	D
1040+59	F	T	F	D	D	D
1057−13	F	F	T	A	S	S
1127+24	F	T	T	D	D	D
1131+16	T	P[a]	T	A	S	S
1158−30	F	F	T	A	S	S
1212−14	F	T	T	A	X	S
1321+13	F	F	T	A	X	S
1323−02	F	T	T	A	S	S
1338−04	T	T	T	D	D	D
1407+42	T	F	T	A	S	S
1448+44	F	T	T	D	D	D
2121−17	T	T	T	D	D	D

[a]See Rose et al. (2011) for full description.

4.1.3 Narrow-line type 1 Seyfert galaxies

Narrow-line type 1 Seyfert galaxies (NLS1) are a subclass of Seyfert galaxies with BLR Balmer emission lines that are relatively narrow ($\mathrm{FWHM}_{\mathrm{H}\beta} < 2000$ km s^{-1}; Osterbrock & Pogge 1985; Véron-Cetty, Véron & Gonçalves 2001). There are several hypotheses surrounding the nature of these objects. One prevailing idea is that NLS1 are AGN with lower than typical black hole masses that are undergoing a phase of rapid accretion (Pounds, Done & Osbourne 1995). In this scenario the NLS1 fall below, but are growing towards, the M–σ correlation (Ferrarese & Merritt 2000); eventually, as they accrete more mass, they will appear as typical Seyfert objects (Mathur 2000).

If the red 2MASS objects are young, recently triggered AGN, then we might expect there to be a relatively large fraction of NLS1 objects in the sample. We checked our sample for NLS1 based on single Gaussian fits to their Hβ lines, to find objects

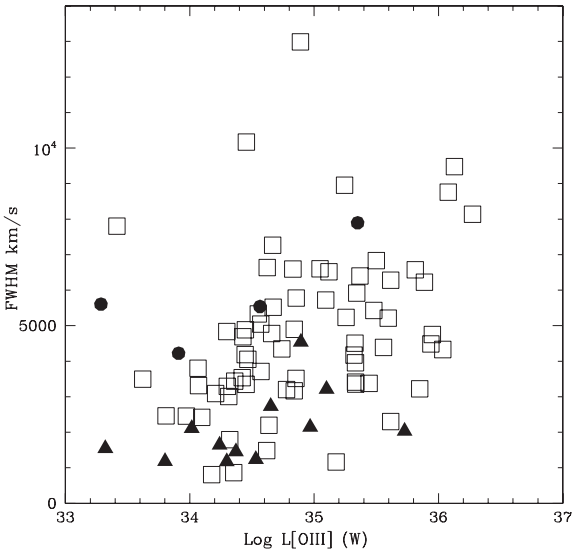

Figure 12. Velocity width (FWHM) of the BLR components plotted against $L_{[O\,III]}$. The 2MASS objects for which broad emission can be confidently separated from the narrow-line emission are indicated by the filled circles, whereas the 2MASS objects for which the broad and narrow emission could not be confidently separated are indicated by the filled triangles. The PG quasar population are indicated by the unfilled squares. All the line measurements are based on single Gaussian fits.

with Hβ or Hα emission-line widths that are below the NLS1 limit (FWHM $<$ 2000 km s^{-1}), but greater than the widths of the [O III] lines. This is consistent with the fitting procedures of Osterbrock & Pogge (1985) and Goodrich (1989). We found that four objects with adequate single Gaussian fits to Hβ have velocity widths consistent with them being NLS1: J0248+14, J0422−18, J0435−06 and J1006+41. These objects have Hβ velocity widths (FWHM) of 1550 ± 20, 1450 ± 120, 1780 ± 70 and 1170 ± 70 km s^{-1}, respectively.

Fig. 13 shows the single Gaussian fits to the Hβ emission lines in these objects. Apart from the line widths, there are two other key properties that are found to be associated with NLS1: [O III] emission lines that are weak relative to the broad Hβ lines ([O III]/H$\beta_{\rm total} < 3$) and the presence of strong Fe II emission (Fe II$_{4570}$/H$\beta_{\rm total} > 0.5$; Osterbrock & Pogge 1985; Goodrich 1989; Véron-Cetty et al. 2001). We find that all four objects with FWHM$_{\rm H\beta} < 2000$ km s^{-1} in our sample also possess these typical NLS1 properties.

Of the AGN in the 2MASS sample, only ∼16 per cent are NLS1 objects, or ∼24 per cent as a fraction of all the broad emission-line objects. This is similar to the fraction of NLS1 found in other samples of broad-line AGN: ∼24 per cent for the unobscured type 1 AGN (Jin et al. 2012a); 11 per cent for the PG quasars (Hao et al. 2005); and ∼15 per cent of all QSOs in SDSS DR3 AGN catalogue (Zhou et al. 2006). Therefore, we conclude that the 2MASS sample does not contain an unusually high proportion of NLS1 objects.

4.2 Balmer decrements and reddening

One possible explanation for the red colours of the 2MASS objects at NIR wavelengths is that their AGN suffer an unusual amount of dust extinction compared with other samples of AGN (e.g. Glikman et al. 2004). In order to investigate this possibility, we have calculated Balmer recombination line decrements for the 2MASS, PG/SDSS and Jin et al. (2012a,b,c) samples to determine whether

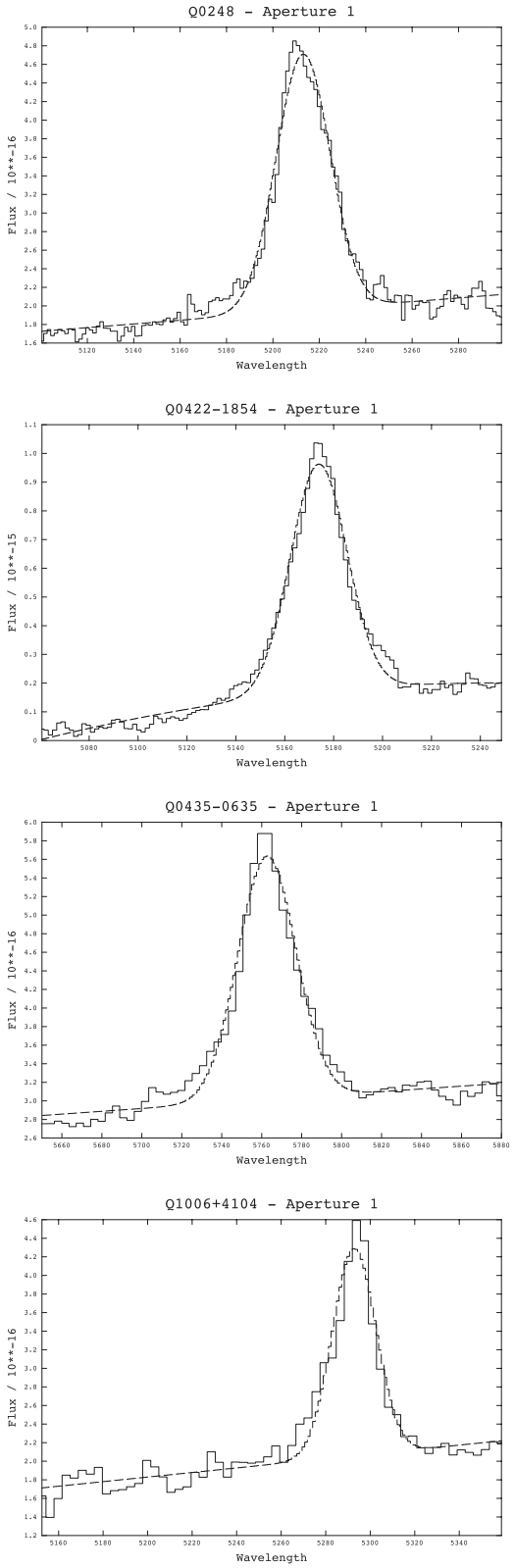

Figure 13. Gaussian fits to the Hβ emission lines of the NLS1 candidates in the 2MASS sample. From top to bottom: J0248+14, J0422−18, J0435−06 and J1006+41. The overall fits to the emission lines are adequate and therefore we use the velocity widths (FWHM) to characterize these objects.

Table 6. The Hα/Hβ Balmer decrements measured for the 2MASS sample. The second column presents the Balmer decrements for the total (BLR + NLR) fluxes. The third and fourth columns present the NLR and BLR Balmer decrements, respectively.

Name	$F_{H\alpha}/F_{H\beta}$ Total	NLR	BLR
J0221+13	–	3.00 ± 0.34	–
J0248+14	7.21 ± 0.64	–	–
J0306−05[a]	–	8.87 ± 2.20	–
J0312+07	5.20 ± 0.45	–	–
J0400+05	7.87 ± 0.51	7.03 ± 0.51	8.07 ± 0.79
J0409+07	2.38 ± 0.46	5.00 ± 0.46	1.67 ± 0.08
J0422−18	4.30 ± 0.35	–	–
J0435−06	3.45 ± 0.43	–	–
J0447−16	8.74 ± 1.48	–	–
J0504−19	–	3.83 ± 0.82	–
J0910+33	–	2.15 ± 0.62	–
J1006+41[b]	5.96 ± 0.28	–	>5.00
J1014+19	5.57 ± 0.79	–	–
J1040+59[b]	12.14 ± 0.57	–	>6.67
J1057−13	–	8.05 ± 0.67	–
J1127+24	4.89 ± 0.46	3.25 ± 0.46	5.38 ± 0.60
J1131+16[c]	–	5.00 ± 0.17	–
J1158−30	–	10.98 ± 0.48	–
J1212−14	4.79 ± 0.93	5.07 ± 0.93	4.71 ± 0.75
J1321+13	–	5.67 ± 0.52	–
J1323−02	4.75 ± 0.87	–	–
J1338−04	3.75 ± 0.69	–	–
J1407+42	–	6.79 ± 0.68	–
J1448+44	4.90 ± 1.21	–	–
J2124−17	2.15 ± 1.19	–	–

[a]Sky line features cut through the region of the Hβ emission line. Results are based on an upper limit measurements for the Hβ emission line, but are presented as a lower limit on the Balmer decrement.
[b]BLR Balmer decrement is based on an upper limit of the Hβ flux and therefore is a lower limit of the Balmer decrement.
[c]The emission flux from Hα is boosted by collisional excitation in this object (Rose et al. 2011).

the 2MASS objects have higher levels of dust extinction than 'typical' blue quasars.

Ideally, Balmer decrements ($F_{H\alpha}/F_{H\beta}$) would be determined for the narrow- and broad-line components of each object separately. However, some objects with a detectable BLR have relatively narrow broad lines (e.g. J1006+41), which makes it difficult to separate the components at the resolution of our spectra (see Section 3.3). Therefore, we have taken two approaches. For the first approach, we used the measured total (broad and narrow) fluxes of the Balmer emission lines. The second approach was to separate the broad and narrow emission components of the blends, where the components could be confidently separated. We only used the total (broad + narrow) Balmer flux measurements for the Jin et al. (2012a) sample, because we were uncertain whether the broad and narrow emission components could be confidently separated in that sample. In addition, when we consider Balmer decrements for the total flux of the Balmer lines, we only use the data for the objects with a detectable BLR, and do not consider the Balmer decrements for the type 2 objects. Balmer decrements for the 2MASS objects are given in Table 6.

Fig. 14 shows histograms of the Balmer decrements ($F_{H\alpha}/F_{H\beta}$) for the combined broad and narrow Balmer emission of the 2MASS

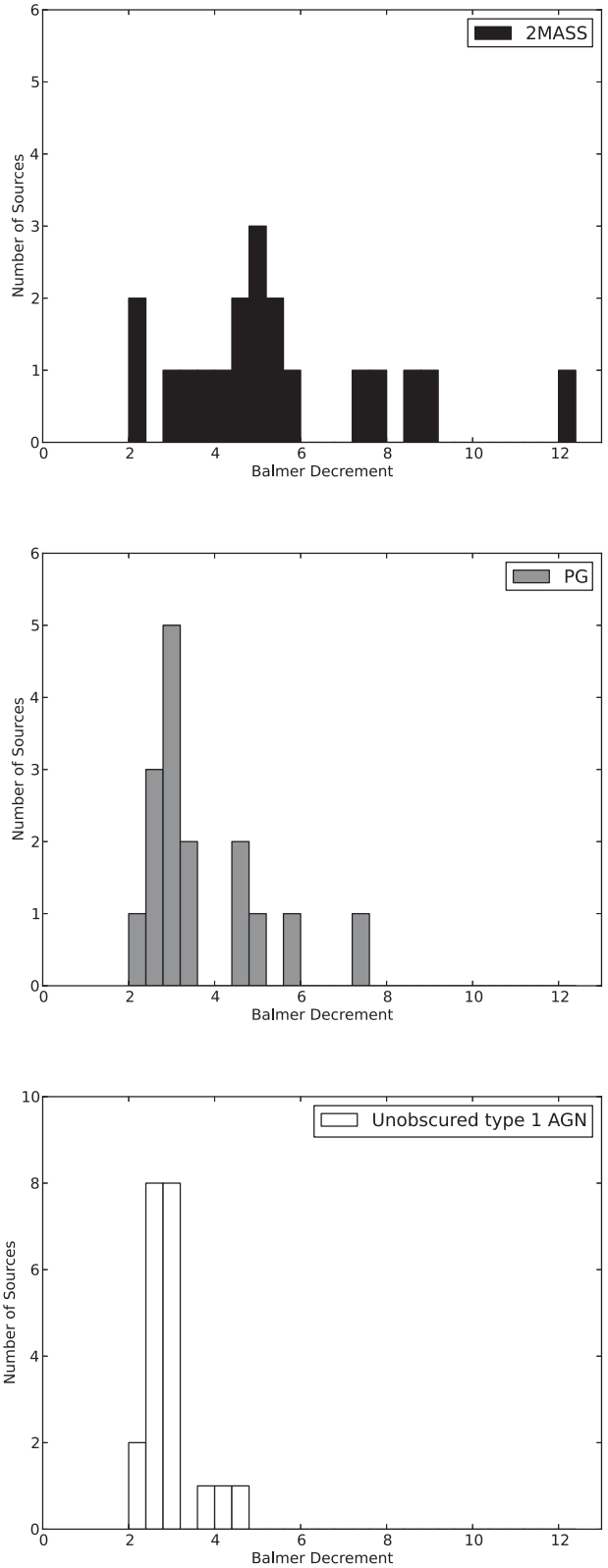

Figure 14. Comparison of the total flux Balmer decrements ($F_{H\alpha}/F_{H\beta}$). The 2MASS population measurements (broad-line objects only) are indicated in black (top), the PG quasar population are shown in grey (middle) and the unobscured type 1 AGN are given in white (bottom). Note that the Balmer decrements are only presented for those objects with broad Balmer emission.

sample (broad-line objects only), the PG/SDSS sample and the unobscured type 1 AGN.

It is clear from this figure that, on average, the 2MASS sample objects have higher $F_{\rm H\alpha}/F_{\rm H\beta}$ ratios than the PG quasars and unobscured type 1 AGN, implying that there is more dust extinction in the 2MASS sample. There is also a significant fraction of objects (5/19) with Balmer decrements that are higher than the most reddened PG quasars. This is reflected in the median $F_{\rm H\alpha}/F_{\rm H\beta}$ ratios: $F_{\rm H\alpha}/F_{\rm H\beta} = 4.9 \pm 0.5$, 3.2 ± 0.4 and 2.8 ± 0.1 for the 2MASS, PG/SDSS and unobscured type 1 objects, respectively.

To put this in context, the Balmer decrements for the 2MASS sample suggest reddening in the range $0.0 \leq E(B-V) \leq 1.2$, with a median $E(B-V) = 0.52 \pm 0.05$, assuming a Case B Hα/Hβ ratio of 3.1 (Gaskell & Ferland 1984). However, although the 2MASS sample displays a significant degree of dust reddening, there are several objects ($\sim$25 per cent of all the broad-line objects) which show very little (if any) significant BLR reddening. These objects include J0312+07, J0409+08, J0435−06, J1338−04 and J2121−17. This is interesting, because it highlights the diverse nature of the 2MASS sample. We further note that three of the objects with low Balmer decrements – J0312+07, J0435−06 and J1338−04 – have $J-K_{\rm S}$ colours just below the $J-K_{\rm S} = 2.0$ limit. Also, J1040+59, an object with one of the highest Balmer decrements, has one of the reddest $J-K_{\rm S}$ colours in the sample ($J-K_{\rm S} = 3.02$). However, overall we do not find a statistically significant correlation between $J-K_{\rm S}$ colours and Balmer decrements for the 2MASS sample.

We have performed Kolmogorov–Smirnov (K-S) tests to check the significance of any differences in the distribution of the Balmer decrements between the samples. We find that we can reject the null hypothesis that the 2MASS sample is drawn from the same parent population as the PG quasars and unobscured type 1 AGN at the 2σ and $>3\sigma$ levels of significance, respectively (the corresponding p values are 0.007 and $<$0.001).

In the cases where it was possible to clearly separate the BLR and NLR components, we find that the Balmer decrements obtained for the BLR components alone are not significantly different from those derived from the total (BLR + NLR) fluxes (see Table 6). Therefore, we do not consider the pure BLR Balmer decrements further in this paper.

When considering the range of reddening found for our 2MASS AGN, our results are consistent with the idea that dust reddening plays a significant role in causing the red NIR colours of the 2MASS objects (see Section 6.1).

4.2.1 Reddening in the NLR

It is also interesting to consider the NLR Balmer decrements for the red 2MASS AGN in which the NLR and BLR components could be clearly separated. The results are presented in Fig. 15. We find that the NLR Balmer decrements cover a similar range to those measured for the BLR (and BLR + NLR combined), with some objects showing evidence for a high degree of reddening, but others showing no significant reddening. We have compared the distributions of the narrow emission-line Balmer decrements for the 2MASS objects and unobscured type 1 AGN using a K-S test and find that we cannot reject the null hypothesis that these samples are drawn from the same parent population, because the test gives a high p value: 0.099. Note that small number statistics preclude a detailed comparison of the NLR Balmer decrements between the 2MASS and PG/SDSS samples. Also, in the case of the NLR it may not be valid to assume Case B recombination for the intrinsic reddened Balmer decrement: our detailed analysis of J1131+16

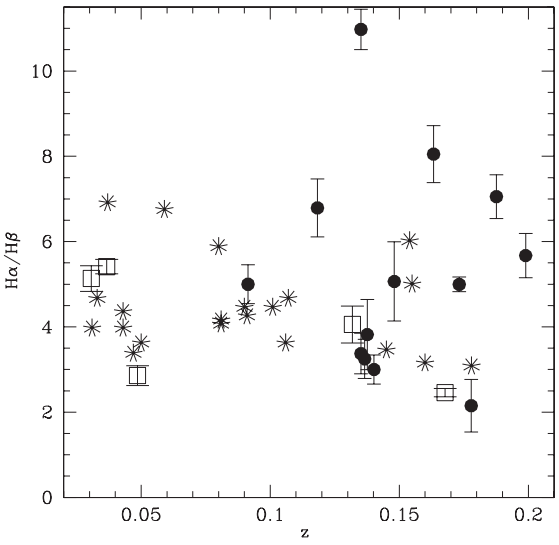

Figure 15. The Balmer decrement ($F_{\rm H\alpha}/F_{\rm H\beta}$) versus redshift, z, for the NLRs of the 2MASS sample. The 2MASS population measurements are indicated by the filled circles, the PG/SDSS quasars are indicated by the unfilled squares and the unobscured type 1 objects are indicated by the asterisks.

(Rose et al. 2011) demonstrates that collisional excitation of the Hα emission line in the partially ionized zone can significantly enhance the Hα/Hβ ratio if the gas densities are high (e.g. if part of the NLR emission originates in the circumnuclear torus).

4.3 Outflows

If the red 2MASS objects truly represent young AGN enshrouded in a cocoon of dust and gas, then we might expect them to show strong evidence for outflows in their spectra, when compared to other types of active galaxies. For example, in models of major galaxy mergers the AGN are triggered as gas and dust is driven by the tidal torques associated with the mergers into the nuclear regions of the galaxies; the AGN accrete at high Eddington rates, and then drive powerful outflows, blowing away the enshrouding dust and gas (Hopkins et al. 2005, 2006; Narayanan et al. 2006).

Fig. 16 shows a histogram of the rest-frame velocity shifts of the broad [O III] components (where detected) relative to those of the narrower components, as calculated from the parameters given in Table 3. The 2MASS objects are plotted along with the PG quasars and the unobscured type 1 AGN for comparison. For the unobscured type 1 AGN, we used the online data tables from Jin et al. (2012a) to determine the outflow properties. For the 2MASS objects, PG quasars and unobscured type 1 AGN, we assume that the narrow component of the [O III] emission represents the host galaxy rest-frame emission, and the broader line emission component the outflow (Holt, Tadhunter & Morganti 2008).

From Fig. 16 it is clear that there are no significant differences between the distributions of the velocity shifts of the samples and, the broad components are predominantly blueshifted in all three samples, with only a few exceptions. We find median velocity shifts of -240 ± 80, -230 ± 50 and -160 ± 30 km s^{-1} for the 2MASS, PG and unobscured type 1 samples, respectively. We have tested the significance of any difference between the distributions of velocity shifts of the samples using a 1D K-S test. Between the 2MASS objects and PG quasars we find a p value of 0.731, and between the 2MASS objects and unobscured type 1 objects we find p value = 0.230. Therefore, we cannot confidently reject the null hypothesis

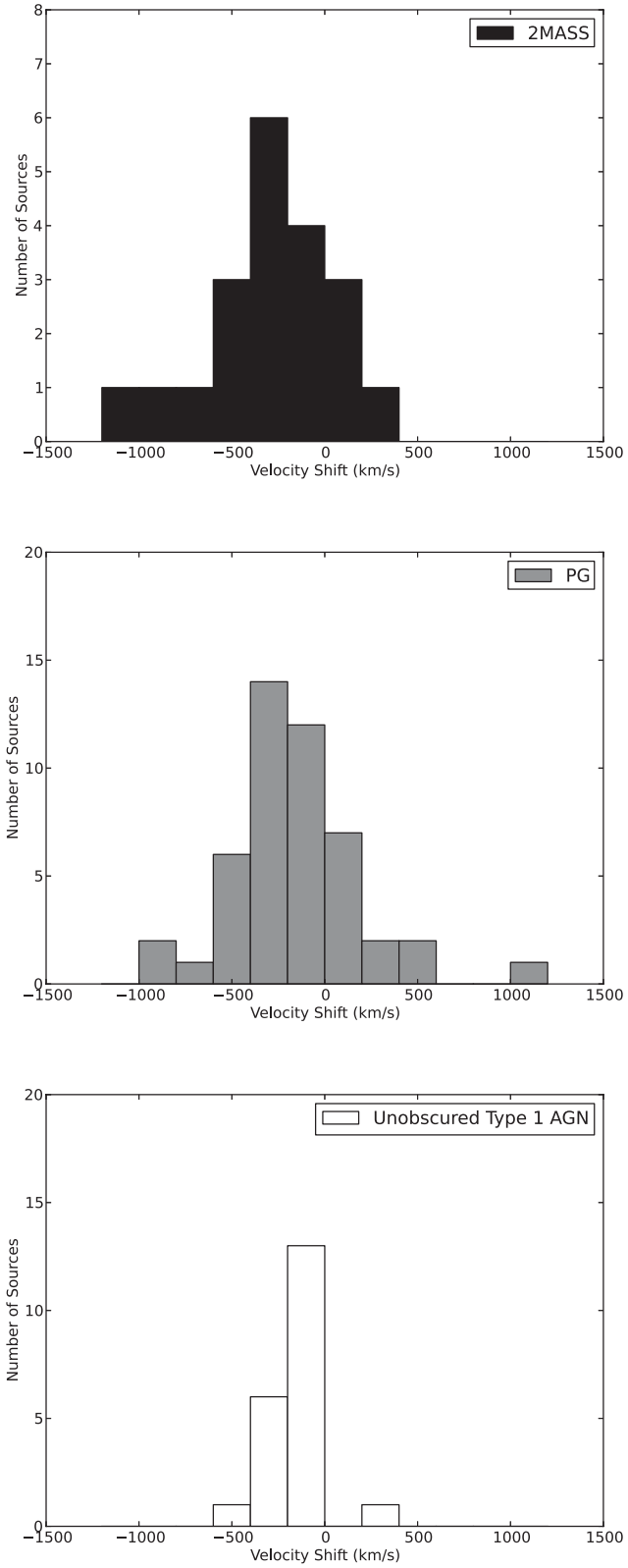

Figure 16. Histogram of the shift of the broad [O III]λ5007 components relative to the narrow components, as measured using DIPSO. The 2MASS measurements are indicated by the black bars (top), the PG quasar population by the grey bars (middle) and the unobscured type 1 AGN by the open bars (bottom).

that these samples are drawn from the same parent population. Note that, although there are no significant differences between the three samples, the most extreme object in all three samples in terms of its shift is a red 2MASS object: J1158−30. This object might be a good candidate for a young AGN.

In addition, in Fig. 17 we plot a histogram of the rest-frame velocity widths (FWHM) of the broad [O III] components. As with the velocity shifts, the widths (FWHM) of all three samples have a comparable range. Again, we have tested for any significant differences between the distribution of velocity widths (FWHM) of the samples using a 1D K-S test. Between the 2MASS objects and PG quasars we find a p value of 0.385, and a p value of 0.089 for the unobscured type 1 AGN. Therefore, we cannot reject the null hypothesis that the samples are drawn from the same parent population when comparing the line widths of the PG quasars and unobscured type 1 AGN with the 2MASS sample.

Fig. 18 shows the outflow velocity plotted against the velocity width (FWHM) of the broad [O III]λ5007 component. We present this figure to further illustrate that there are no significant differences between the [O III] emission-line kinematics of the samples. We have also tested for any significant difference between the populations using a 2D K-S test (Peacock 1983; Fasano & Franceschini 1987). Again, we find no evidence for significant differences between the samples ($p > 0.05$).

One important caveat when considering these results is that the emission-line kinematics may be affected by the orientation of the AGN. One possibility is that our line of sight to the type 2 AGN is at a larger angle to the torus axis than type 1 AGN (as suggested by the orientation-based unified schemes). Therefore, due to projection effects the measured blueshifts of the broad components might be lower in the type 2 than in the type 1 objects. Alternatively, it is possible that the torus obscures the narrow-line outflows from our direct line of sight in the type 2 objects. However, comparisons between the NLR kinematics of type 1 and 2 AGN show no clear differences (e.g. Whittle 1985; Nelson & Whittle 1995).

5 BLACK HOLE AND ACCRETION PROPERTIES

Further insights into the nature of the red 2MASS objects can be obtained by studying the SMBH and accretion properties of the sample. Young, dust enshrouded objects are expected to have higher than average accretion rates, because there is more gas available for accretion (e.g. see Di Matteo, Springel & Hernquist 2005).

To determine the accretion properties, we must first determine the black hole masses of the objects. In this section, we use the broad Balmer emission-line properties to determine virial black hole masses and Eddington ratios for the 2MASS sample, the PG sample and the unobscured type 1 AGN.[5] Any significant differences in the Eddington ratios between the samples could indicate differences in their evolutionary stage.

To determine virial black hole masses, we have used the relationships between the Balmer emission and black hole mass from

[5] For consistency, we use the Hβ luminosities and velocity widths (FWHM) provided in Jin et al. (2012a) to determine the black hole masses, bolometric and Eddington luminosities of the unobscured type 1 AGN sample ($L_{\mathrm{H}\beta}$ and $\mathrm{FWHM}_{\mathrm{H}\beta}$ are flux weighted means of the intermediate and broad components of the Hβ emission lines). Note that, the data used from Jin et al. (2012a) is not corrected for extinction. This is reasonable as the sample is selected to be unreddened.

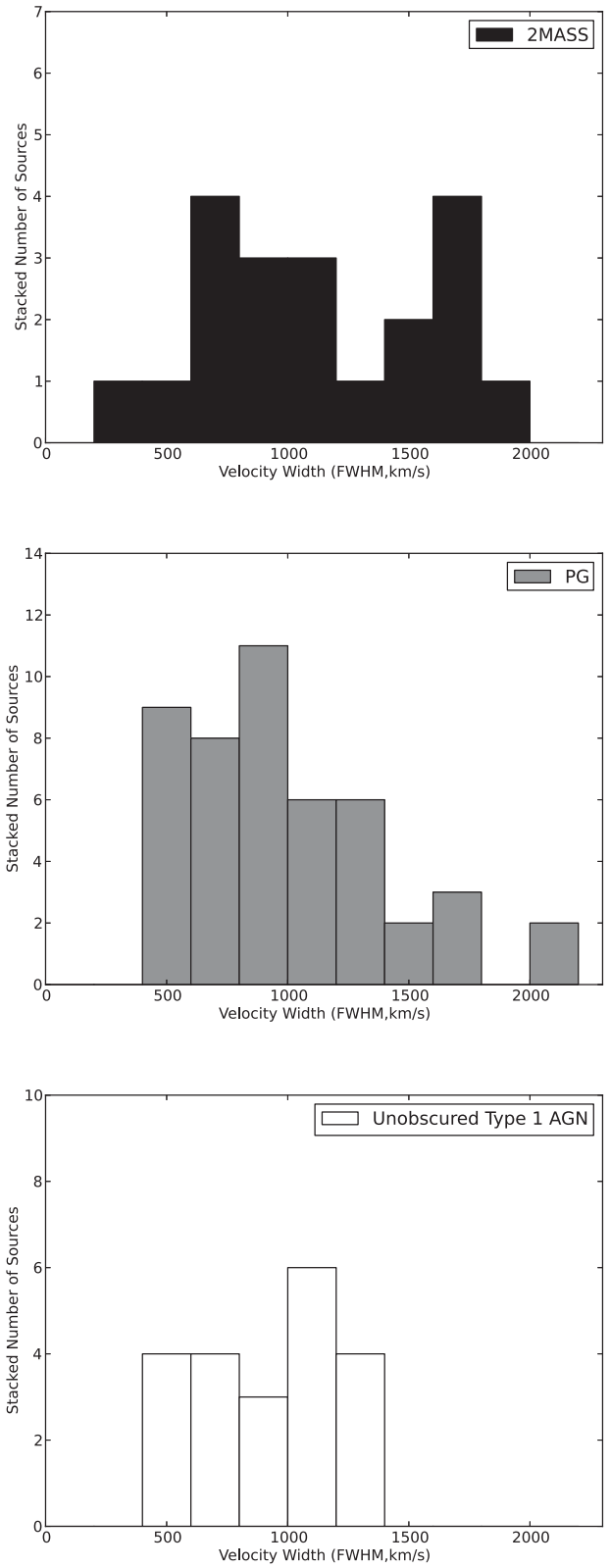

Figure 17. Histogram of the instrumentally corrected velocity widths (FWHM, km s^{-1}) of the broad [O III]λ5007 component, as measured using DIPSO. The 2MASS measurements are indicated by the black bars (top), the PG quasar population by the grey bars (middle) and the unobscured type 1 AGN by the open bars (bottom).

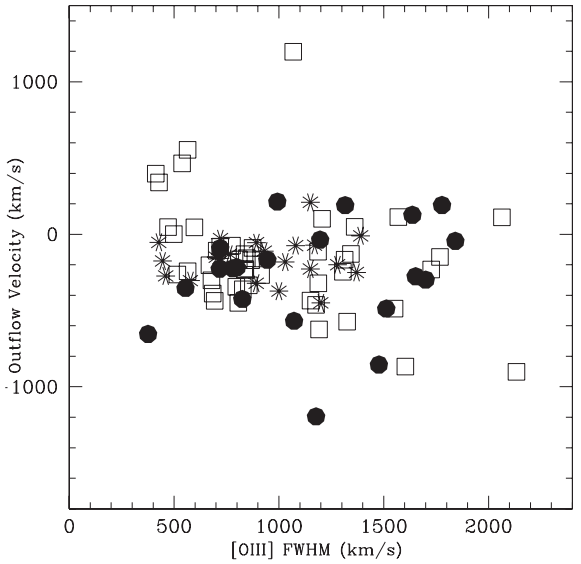

Figure 18. Velocity shift (km s^{-1}) plotted against the velocity width at FWHM (km s^{-1}) of the broad [O III]λ5007 components as measured by DIPSO. The 2MASS population measurements are indicated by the filled circles, the PG quasar population are indicated by the unfilled squares and the unobscured type 1 AGN are indicated by the asterisks.

Greene & Ho (2005), which are based on correlations between the AGN bolometric luminosities ($L_{\rm BOL}$), Balmer line luminosities and line widths (FWHM) (see Greene & Ho 2005 equations 6 and 7). We use equation 7 for most cases where we can use the broad Hβ emission lines, minimizing any degeneracies due to blending with other emission lines (e.g. [N II] with Hα). In cases where the Hβ broad emission is not detectable, we used the Hα broad emission with equation 6 instead.

We fitted the broad Hβ emission with the minimum number of Gaussian components required to obtain an adequate fit to the emission from the BLR, and took a flux weighted mean of the FWHM, consistent with the method of Greene & Ho (2005). Where possible, we corrected the BLR fluxes for extinction, and in cases where we could not confidently separate the broad and narrow emission, we used the total Balmer decrement measurements for the extinction correction. Note that, while our approach is consistent with that outlined in Greene & Ho (2005) when measuring the broad Hβ emission, problems with the separation of the broad and narrow emission in the objects where we could not separate the components may potentially have an effect on the line width measurements. Also, for the cases where we estimated an upper limit on the broad Hβ flux, we used the lower limiting estimate of the extinction to find a lower limit on the SMBH mass, and therefore an upper limit on the Eddington ratio. The 2MASS objects have virial SMBH masses in the range $7.2 < \log_{10}[M_{\rm BH}] < 9.2\,{\rm M}_{\odot}$.

As well as making virial SMBH estimates based on the broad emission-line properties, for comparison we have also used the absolute R-band magnitudes (M_R) of the host galaxies of the 2MASS sample taken from Hutchings et al. (2003). These estimates have the advantage of being free from any degeneracies caused by the blending of the emission lines from the BLR and the NLRs of the sample. In addition, masses can be estimated for all the sources, rather than just the sources with an observable BLR. To make these estimates we used the relation given in McLure & Dunlop (2001), which takes advantage of the correlation between black hole mass and host galaxy bulge luminosity, to determine the SMBH masses.

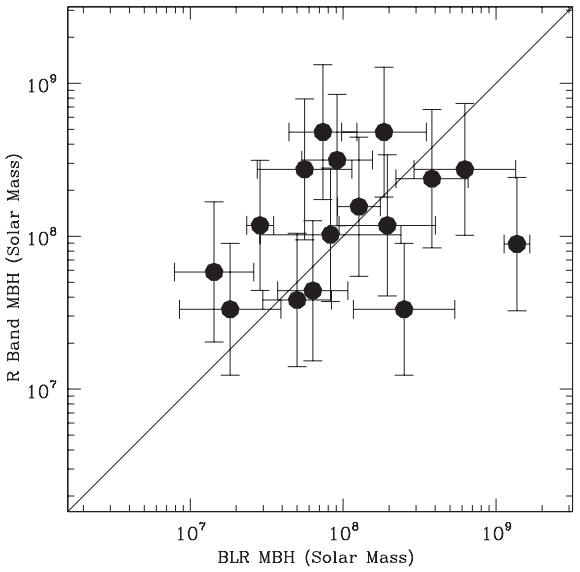

Figure 19. A comparison of the SMBH mass estimates for the 2MASS AGN. We plot the mass estimates based on the *R*-band magnitudes against the virial mass estimates based on the broad Balmer emission lines. In addition, we have plotted a line showing a one to one relationship for the black hole masses. The mass estimates obtained from the *R*-band magnitudes are higher on average than those obtained from the BLR measurements.

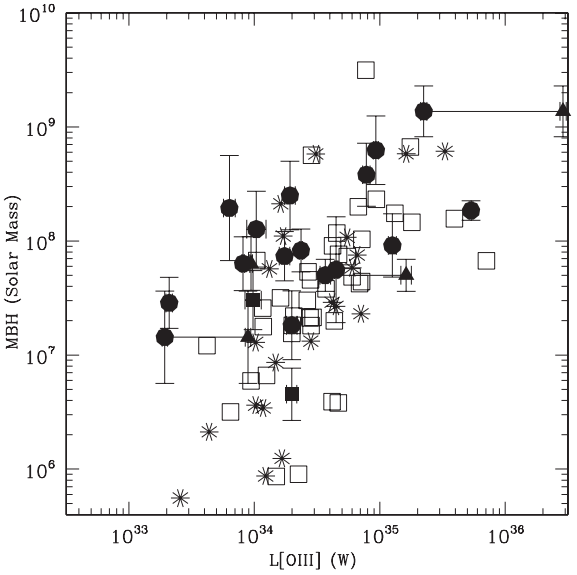

Figure 20. Virial black hole mass ($M_\odot$) plotted against $L_{[O\,III]}$ (W). The filled circles and triangles represent the 2MASS sample. The circles represent black hole masses estimated using Hβ emission and the filled squares are based on the Hα emission. Where possible, we correct $L_{[O\,III]}$ for reddening, these estimates are represented by the filled triangles and are joined to their uncorrected counterparts by a straight line. The unfilled squares represent the black hole mass estimates of the PG sample and the asterisks indicate the type 1 AGN estimates.

Fig. 19 shows the SMBH mass estimates from the *R*-band magnitudes plotted against the masses calculated using the properties of the BLR. In addition, we have plotted a line showing a one-to-one relationship between the black hole masses. While some objects show good agreement between the two estimates, there is a large scatter which is reflected in the uncertainty of the median ratio ($M^{SMBH}_{virial}/M^{SMBH}_{R-band}$): 0.81 $\pm$ 0.81. In cases where the virial mass estimates are lower than the *R*-band estimates, orientation/geometric and/or reddening effects could potentially lead to the Balmer fluxes, velocity widths and SMBH masses being underestimated. Alternatively, the *R*-band measurements may be contaminated by light from the discs of the host galaxies, leading to overestimates of the SMBH masses. Certainly, at least one object in our sample – J1131+16 – has a strong disc component (Rose et al. 2011). However, in cases where the virial masses are higher, the flux of the BLR may be overestimated because of an inaccurate measurement in the broad Hα flux due to blending with the narrow Hα+[N II] lines, which could lead to an overestimation of the level of extinction.

Fig. 20 shows the virial black hole masses plotted against $L_{[O\,III]}$ for the 2MASS and comparison samples, where the uncertainties are only plotted for the 2MASS objects for clarity. We do not plot the *R*-band black hole mass estimates because we do not have *R*-band magnitudes for the comparison samples, and we want to present the comparisons between mass estimates which have been determined via the same method. In addition, Table 7 shows the individual SMBH masses of the 2MASS sample. Overall, from this figure it is clear that the black hole masses of the PG quasars (unfilled squares) and unobscured type 1 AGN (asterisks) are generally lower than the 2MASS objects (filled symbols) of equivalent [O III] luminosity. Potentially, this difference can be explained in terms of extinction effects: in the cases of the few objects with virial mass estimates for which we have been able to correct $L_{[O\,III]}$ for extinction in the NLR, the extinction correction moves the points on to the main correlation defined by the PG quasars and unobscured type 1 objects.

Alternatively, the black hole masses of the 2MASS objects could be genuinely higher than those of the PG quasars and unobscured type 1 AGN of similar intrinsic power. In this context, we note that the recent study of Canalizo et al. (2012) measured black hole masses and host galaxy properties for 29 red 2MASS AGN with $0.17 < z < 0.37$, finding that the majority of red 2MASS AGN also have significantly more massive black hole masses than the masses of black holes in local AGN. However, we remain cautious in our interpretation of the derived black hole masses for our 2MASS sample because of the uncertainty surrounding the extinction corrections.

In terms of estimating the Eddington ratio (L_{BOL}/L_{EDD}), we used $L_{[O\,III]}$ to calculate the bolometric luminosities of the AGN, rather than the AGN continuum, because the [O III] emission line is well detected in all the objects, whereas the AGN continuum emission is subject to reddening effects and potential contamination by the host stellar continuum. L_{BOL} was determined from $L_{[O\,III]}$ using the relationship $L_{BOL} = 3500L_{[O\,III]}$ (Heckman et al. 2004).

Fig. 21 shows the Eddington ratios plotted against L_{BOL}. Once again the uncertainties are only plotted for the 2MASS objects for clarity. We present Eddington ratios for all possible objects in the 2MASS sample without correcting [O III] for dust extinction (filled circles) and, where possible, we also show the Eddington ratios following the correction of the [O III] luminosity for dust extinction (filled triangles), connecting both sets of estimates with a straight line. It is clear that, for the four objects in which we can measure reddening accurately, reddening has a significant effect on the Eddington ratio. There is an obvious, large scatter in Eddington ratios for all the samples: the 2MASS objects have ratios in the range: $0.009 < L_{BOL}/L_{EDD} < 0.91$. The median ratio for the 2MASS sample is 0.05 $\pm$ 0.05, without correcting [O III] for reddening and 0.08 $\pm$ 0.04 in the reddening corrected case. In comparison, the PG quasar sample (unfilled squares) and the unobscured type 1 AGN sample (asterisks) have median ratios of 0.22 $\pm$ 0.12 and

Table 7. Virial SMBH masses and Eddington ratio results for the 2MASS sample. Values presented in brackets are for those objects where $L_{\rm BOL}$ has been corrected for dust extinction.

Name	M_R $\log_{10}[M_{\rm SMBH}]$ ($M_\odot$)	Virial $\log_{10}[M_{\rm SMBH}]$ ($M_\odot$)	$(L_{\rm BOL}/L_{\rm EDD})$
J0221+13	8.19 ± 0.43	–	–
J0248+14	8.07 ± 0.44	7.46 ± 0.09	0.020 ± 0.005
J0306−05	8.25 ± 0.43	–	–
J0312+07	8.07 ± 0.44	8.29 ± 0.32	0.009 ± 0.001
J0400+05[a]	7.95 ± 0.44	9.14 ± 0.08	$0.056(0.585) \pm 0.009(0.125)$
J0409+07[a]	7.58 ± 0.46	7.70 ± 0.05	$0.204(0.901) \pm 0.025(0.112)$
J0422−18	8.01 ± 0.44	7.92 ± 0.11	0.079 ± 0.024
J0435−06	8.68 ± 0.41	7.87 ± 0.26	0.065 ± 0.003
J0447−16	8.19 ± 0.43	8.10 ± 0.11	0.023 ± 0.007
J0504−19	8.01 ± 0.44	–	–
J0910+33	7.83 ± 0.45	–	–
J1006+41[b]	7.52 ± 0.46	7.26 ± 0.10	0.302 ± 0.105
J1014+19	8.44 ± 0.42	8.80 ± 0.13	0.041 ± 0.014
J1040+59[b]	7.52 ± 0.46	8.40 ± 0.11	0.021 ± 0.007
J1057−13	7.77 ± 0.45	–	–
J1127+24[a]	7.64 ± 0.45	7.80 ± 0.10	$0.036(0.041) \pm 0.019(0.0010)$
J1131+16	8.31 ± 0.43	–	–
J1158−30	8.25 ± 0.43	–	–
J1212−14[a]	7.77 ± 0.45	7.16 ± 0.18	$0.037(0.172) \pm 0.020(0.090)$
J1321+13	7.52 ± 0.46	–	–
J1323−02	8.38 ± 0.42	8.58 ± 0.16	0.057 ± 0.026
J1338−04	8.50 ± 0.42	7.96 ± 0.26	0.383 ± 0.025
J1407+42	7.95 ± 0.44	–	–
J1448+44	8.44 ± 0.42	7.75 ± 0.21	0.222 ± 0.137
J2124−17	8.68 ± 0.41	8.27 ± 0.04	0.802 ± 0.068

[a]The NLR of this object has been corrected for dust extinction.
[b]$M_{\rm SMBH}$ and therefore $L_{\rm EDD}$ are calculated using broad Hα emission as opposed to Hβ.

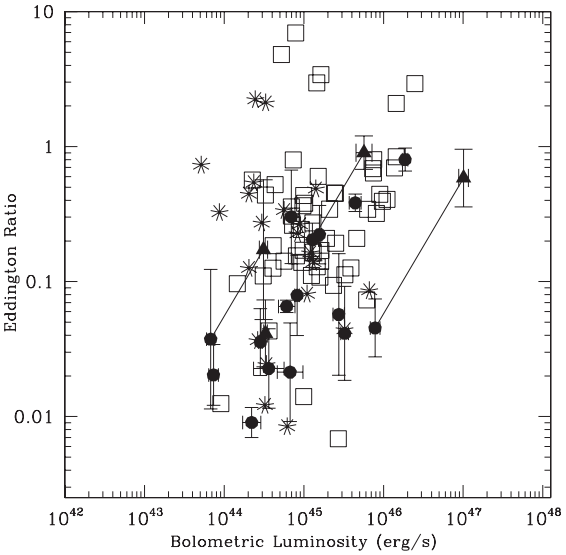

Figure 21. Eddington ratio plotted against $L_{\rm BOL}$ (erg s^{-1}) based on measurements of $L_{[\rm O\,III]}$ and virial black hole mass estimates. The filled circles represent the 2MASS objects where $L_{[\rm O\,III]}$ has not been corrected for dust extinction. For objects which could be corrected for dust extinction, we represent them with the filled triangles and join them to their respective estimates where no correction has been made. The unfilled squares represent the PG quasars and the asterisks represent the unobscured type 1 objects.

0.23 ± 0.14, respectively; the large uncertainties reflect the large scatter in Eddington ratio. These ratios are all consistent within 2σ of the uncertainties. Note that, if we could correct for NLR reddening in *all* the objects, the median ratio for the 2MASS objects would likely increase to a value closer to that measured for the PG quasar and unobscured type 1 AGN samples. Clearly, there is no evidence that the 2MASS objects have Eddington ratios that are significantly higher than those of the comparison samples.

6 DISCUSSION

6.1 Moderately reddened objects

A key result from this study is that many of the red 2MASS AGN have moderate amounts of dust extinction when compared to the comparison samples ($0.2 < E(B-V) < 1.2$); the reddening values we measure are consistent with those determined for other samples of red 2MASS AGN [$0.1 < E(B-V) < 3.2$; Glikman et al. 2004, 2007, 2012; Shi et al. 2007; Urrutia et al. 2008, 2009, 2012; Georgakakis et al. 2009; Kuraszkiewicz et al. 2009a,b; Glikman 2011; Canalizo et al. 2012]. Therefore, it is possible that the 2MASS AGN have red $J-K_{\rm S}$ colours because dust extinction reduces the J-band flux relative to the K-band flux such that the F_K/F_J flux ratio is higher than a typical AGN. In Paper II we will show that for an AGN with intrinsic NIR colours that are typical of the PG quasars and the unobscured type 1 AGN ($J-K_{\rm S} \sim 1.70$), we would require only a moderate level of reddening of $E(B-V) > 0.8$ in order to give $J-K_{\rm S} > 2.0$ – this level of extinction is measured for 29 per cent of the 2MASS AGN with broad Balmer emission lines.

Rather than the red NIR colours being a result of dust extinction from a natal cocoon of dust, it is possible that the obscuring dust is located in the outer layers of the torus, and that we are observing these objects at an angle where our line of sight grazes the edge of the torus, leading to the observed red colours. However, such

Table 8. Basic properties of red AGN samples.

Sample	Size	z	Data used in study	Key selection criteria
This paper	29	$0.06 < z < 0.28$	Optical spectra	$J - K_S \gtrsim 2.0$, selected from Hutchings et al. (2003)
Glikman et al. (2004, 2007, 2012) and Glikman (2011)	120	$0.1 < z < 2.5$	Optical and IR spectra	$J - K_S \geq 1.7$ and $R - K \geq 4.0$, selected by cross-correlating the 2MASS PSC with the FIRST radio catalogue
Georgakakis et al. (2009)	10	$0.29 < z < 3.1$	UV–FIR SED fitting	$J - K_S \geq 1.5$ and $R - K \geq 5.0$, selected by cross-correlating the 2MASS PSC with SDSS DR3 spectra
Urrutia et al. (2008, 2009, 2012)	13	$0.1 < z < 1.0$	Optical spectra	Selected from the Glikman et al. (2007) sample
Shi et al. 2007	25	$0.08 < z < 0.37$	IR Spectra	$J - K_S \gtrsim 2.0$, selected from Cutri et al. (2001)
Kuraszkiewicz et al. (2009a,b)	44	$0.07 < z < 0.37$	X-ray-FIR SED fitting, PCA analysis	$J - K_S > 2.0$ and $B - K_S > 4.3$
Canalizo et al. (2012)	9	$0.13 < z < 0.37$	Optical/NIR spectroscopy, *HST* images	$J - K_S > 2.0$ and $M_K \lesssim -25$
Marble et al. (2003)	29	$0.13 < z < 0.6$	*HST* images	$J - K_S > 2.0$ and $M_K \lesssim$ -23
Smith et al. (2002)	20	$0.06 < z < 0.6$	Optical broad-band polarimetry	$J - K_S > 2.0$ and $M_K \lesssim -23$

modest levels of reddening could also be produced by dust on a kiloparsec scale in the discs of the host galaxies.

Alternatively, rather than moderately extinguished AGN, it is possible that some of these objects are genuine type 2 objects in which the torus completely extinguishes the broad-line AGN in the optical and shorter wavelength NIR bands. In this case, the level of extinction is expected to be much higher ($A_V > 10$) than that indicated by the Balmer decrements in the NLR because, while the SMBH and BLR are completely obscured at optical wavelengths by the torus, the NLR extends beyond the scale of the torus and is therefore relatively unaffected. In this case, due to the much higher levels of extinction caused by the torus, their $J - K_S$ colours should be much redder than is observed. Indeed, from our work in Paper II, we find that $A_v > 5$ would produce $J - K_S > 3.00$, a level only found for the type 2 2MASS object J1307+23 (excluded from the main study of this paper), but not for any of the other type 2 objects in our sample. However, the integrated NIR colours of the heavily extinguished type 2 objects could be made bluer if the host galaxies make a significant contribution in the NIR, because the colours of typical unreddened stellar populations are relatively blue at such wavelengths.

Finally, we note that dust extinction is not the only explanation for the red NIR colours of the 2MASS objects. Some objects in our sample show relatively modest levels of extinction based on their BLR Balmer decrements, and have optical continuum shapes that appear similar to UV-/optical-selected AGN (e.g. J2124−17). Rather than moderate levels of dust extinction in such cases, a relatively large covering factor for the hot dust ($T \sim 1500$ K) could also result in red $J - K_S$ colours. Emission from hot dust in the torus becomes significant at wavelengths which coincide with the *K* band. Therefore, a larger than average covering factor for this hot dust could increase the flux measured in the *K* band relative to that of the *J* band (likely dominated by accretion disc emission), thus, producing the red $J - K_S$ colours measured for the 2MASS sample.

All of these possibilities will be explored further in Paper II, where we will model the NIR to mid-IR spectral energy distributions (SEDs) of the 2MASS objects with varying the level of extinction, dust covering factors and host galaxy contributions.

6.2 Young, dust enshrouded objects?

There have been several studies of red 2MASS AGN in the past that have focused on different wavelength regions of the SEDs of the population (e.g. X-ray, UV, optical or IR). In this section, we outline the basic properties and findings of these studies, and compare them with the results obtained in this paper, in order to determine the nature of our red, low-z, 2MASS AGN sample. The basic properties of the samples used for the previous studies are summarized in Table 8.

Many of these past studies conclude that the red 2MASS quasars are young, dust-enshrouded, transitional objects. This conclusion is based on several lines of evidence, including a high rate of morphological disturbance of the host galaxies (Urrutia et al. 2008), a relatively high rate of occurrence low-ionization broad absorption lines (LoBALs; Urrutia et al. 2009), evidence for enhanced star formation rates compared to typical UV-/optical-selected AGN (Shi et al. 2007; Georgakakis et al. 2009) and high Eddington ratios for the gas being accreted by the central SMBHs (Urrutia et al. 2012).

In contrast, although the results from our local 2MASS AGN sample agree with these previous studies in the sense that we determine the same moderate levels of reddening, we find no strong evidence that these are young quasars based on their [O III] outflow properties, the incidence of NLS1, and the distribution of Eddington ratios. Indeed, the properties of our 2MASS sample appear similar to those of the samples of UV-/optical-selected quasars in the local Universe.

The apparent discrepancy between the conclusions of our study and the previous studies that identify the red 2MASS objects as young, transition objects may be due to different selection criteria. In particular, the Glikman et al. (2004, 2007, 2012), Glikman (2011), Georgakakis et al. (2009) and Urrutia et al. (2008, 2009, 2012) samples extend up to much higher redshifts than our local sample, include optical colour selection criteria as well as NIR colour selection, and some require the objects to have broad lines; in addition, Glikman et al. (2004, 2007, 2012) and Glikman (2011) require detection of the objects in the FIRST radio survey. Such

selection criteria favour more extreme objects that are more likely to be genuinely young and dust enshrouded.

In this context, it is notable that other studies of 2MASS AGN which are based on lower redshift samples and/or samples selected without additional optical colour criteria (the bottom four entries in Table 8), agree with the conclusions of our investigation, albeit using different analysis techniques:

– from X-ray to far-infrared (FIR) SED studies, and PCA analysis of a population of red 2MASS AGN, Kuraszkiewicz et al. (2009a,b) conclude that the red 2MASS AGN are not observed at a younger evolutionary phase than other local samples;

– using *I*-band *Hubble Space Telescope* (*HST*) images to study the host galaxies of red 2MASS AGN, and comparing their findings to the PG quasars and a sample of ULIRGs, Marble et al. (2003) find no indication that red 2MASS AGN represent young, dust enshrouded, transitional objects;

– by comparing optical broad-band polarimetry results of red 2MASS AGN, PG quasars and broad absorption line (BAL) AGN, Smith et al. (2002) find that overall 2MASS AGN show relatively high levels of polarization ($P > 3$ per cent), consistent with the idea that orientation/obscuration effects are responsible for the red NIR colours.

These comparisons between the previous studies of the red 2MASS AGN emphasize the sensitivity of the conclusions to the precise selection criteria employed for the particular samples. However, it seems unlikely that the majority of low-redshift 2MASS AGN that are selected solely on the basis of NIR colour [$(J - K) \geq 2$] are young, transitional objects.

7 CONCLUSION AND FUTURE WORK

In this work, we present a study of the optical spectra of a representative sample of 29 nearby ($z < 0.28$) 2MASS-selected AGN with red NIR colours ($J - K_S \gtrsim 2.0$). We compare the results from this sample with those obtained for comparison samples of PG quasars and unobscured type 1 AGN. We find the following.

(i) Overall the local 2MASS AGN population show significantly higher reddening than samples of UV-/optical-selected AGN. However, while some objects are highly reddened ($E(B - V) = 1.2$), others show relatively little (if any) reddening.

(ii) The velocity shifts and widths of the [O III] lines of the red 2MASS AGN are not significantly larger than those of the comparison samples.

(iii) The Eddington ratios of the 2MASS AGN and the incidence of NLS1-type objects are comparable with those of 'typical' AGN.

These results do not support the view that the local red 2MASS AGN represent young quasars in a transitional phase, where the AGN are emerging from their natal cocoons of gas and dust. However, they are consistent with the idea that these objects are reddened either by obscuring dust in the outer layers of the circumnuclear tori, or by dust in the kpc-scale discs of the host galaxies.

In Paper II, we will focus on the NIR properties of this sample of red 2MASS AGN and investigate the origin of their red $J - K_S$ colours.

ACKNOWLEDGEMENTS

We would like to thank the referee for useful comments and suggestions. MR acknowledges support in the form of an STFC PhD studentship. The authors thank T. Boroson for kindly supplying the spectra of the Boroson & Green (1992) sample. The authors acknowledge the data analysis facilities provided by the Starlink Project, which is run by CCLRC on behalf of PPARC. The William Herschel Telescope and its service programme are operated on the island of La Palma by the Isaac Newton Group in the Spanish Observatorio del Roque de los Muchachos of the Instituto de Astrofísica de Canarias. This publication makes use of data products from the Two Micron All Sky Survey, which is a joint project of the University of Massachusetts and the Infrared Processing and Analysis Center/California Institute of Technology, funded by the National Aeronautics and Space Administration and the National Science Foundation. This research has made use of the NASA/IPAC Extragalactic Database (NED) which is operated by the Jet Propulsion Laboratory, California Institute of Technology, under contract with the National Aeronautics and Space Administration. Funding for SDSS-III has been provided by the Alfred P. Sloan Foundation, the Participating Institutions, the National Science Foundation and the US Department of Energy Office of Science.

REFERENCES

Antonucci R., 1993, ARA&A, 31, 473
Antonucci R. R. J., Miller J. S., 1985, ApJ, 297, 621
Baldwin J., Phillips M., Terlevich R., 1981, PASP, 93, 5
Bellamy M. J., Tadhunter C. N., Morganti R., Wills K. A., Holt J., Taylor M. D., Watson C. A., 2003, MNRAS, 344, 80
Bian W., Gu Q., Zhao Y., Chao L., Cui Q., 2006, MNRAS, 372, 876
Boroson T. A., Green R. F., 1992, ApJS, 80, 109
Bruzual G., Charlot S., 2003, MNRAS, 344, 1000
Calzetti D., Armus L., Bohlin R. C., Kinney A. L., Koornneef J., Storchi-Bergmann Th., 2000, ApJ, 533, 682
Canalizo G., Wold M., Hiner K. D., Lazarova M., Lacy M., Aylor K., 2012, ApJ, 760, 38
Cutri R. M., Nelson B. O., Kirkpatrick J. D., Huchra J. P., Smith P. S., 2001, in Clowes R., Adamson A., Bromage G., eds, ASP Conf. Ser. Vol. 232, The New Era of Wide Field Astronomy. Astron. Soc. Pac., San Francisco, p. 78
Cutri R. M., Nelson B. O., Francis P. J., Smith P. S., 2002, in Green R. F., Khachikian E. Ye., Sanders D. B., eds, ASP Conf. Ser. Vol. 284, IAU Colloq. 184: AGN Surveys. Astron. Soc. Pac., San Francisco, p. 127
Dain S., Lousto C. O., Zlochower Y., 2008, Phys. Rev. D, 78, 4039
Di Matteo T., Springel V., Hernquist L., 2005, Nat, 433, 604
Dicken D., Tadhunter C., Axon D., Morganti R., Inskip K. J., Holt J., González Delgado R., Groves B., 2009, ApJ, 694, 268
Dickson R., Tadhunter C., Shaw M., Clark N., Morganti R., 1995, MNRAS, 273, 29
Fasano G., Franceschini A., 1987, MNRAS, 225, 155
Ferrarese F., Merritt D., 2000, ApJ, 539, 9
Francis P. J., Whiting M. T., Webster R. L., 1999, Publ. Astron. Soc. Aust., 17, 56
Gaskell C. M., Ferland G. J., 1984, PASP, 96, 393
Georgakakis A., Clements D. L., Bendo G., Rowan-Robinson M., Nandra K., Brotherton M. S., 2009, MNRAS, 394, 533
Glikman E., 2011, PoS(Bash11)009
Glikman E., Gregg M. D., Lacy M., Helfand D. J., Becker R. H., White R. L., 2004, ApJ, 607, 60
Glikman E., Helfand D. J., White R. L., Becker R. H., Gregg M. D., Lacy M., 2007, ApJ, 667, 673
Glikman E. et al., 2012, ApJ, 757, 51
Goodrich R. W., 1989, ApJ, 342, 224
Greene J. E., Ho L. C., 2005, ApJ, 630, 122
Hao C. N., Xia X. Y., Mao S., Wu H., Deng Z. G., 2005, ApJ, 625, 78
Hazard C., Mackey A. J., Shimmins A. J., 1963, Nat, 197, 1037
Heckman T. M., Kauffmann G., Brinchmann J., Charlot S., Tremonti C., White S. D. M., 2004, ApJ, 613, 109

Holt J., Tadhunter C., Morganti R., Bellamy M., González Delgado R. M., Tzioumis A., Inskip K. J., 2006, MNRAS, 370, 1633
Holt J., Tadhunter C. N., González Delgado R. M., Inskip K. J., Rodriguez Zaurin J., Emonts B. H. C., Morganti R., Wills K. A., 2007, MNRAS, 381, 611
Holt J., Tadhunter C. N., Morganti R., 2008, MNRAS, 387, 639
Hopkins P. F., Hernquist L., Cox T. J., Di Matteo T., Martini P., Robertson B., Springel V., 2005, ApJ, 630, 705
Hopkins P. F., Hernquist L., Cox T. J., Di Matteo T., Robertson B., Springel V., 2006, ApJS, 163, 1
Howarth I. D., 1983, MNRAS, 203, 301
Howarth I. D., Murray J., Mills D., Berry D. S., 2004, Starlink User Note 50.24 (Swindon: PPARC) (http://www.starlink.rl.ac.uk/star/docs/sun50.htx/sun50.html)
Hutchings J. P., Maddox N., Cutri R. M., Nelson B. O., 2003, AJ, 126, 63
Jin C., Ward M., Done C., Gelbord J., 2012a, MNRAS, 420, 1825
Jin C., Ward M., Done C., 2012b, MNRAS, 422, 3268
Jin C., Ward M., Done C., 2012c, MNRAS, 425, 907
Kewley L. J., Groves B., Kauffmann G., Heckman T., 2006, MNRAS, 372, 961
Kim D.-C., Sanders D. B., 1998, ApJS, 119, 41
Kovačević J., Popović L. Č., Dimitrijević M. S., 2010, Mem. Soc. Astro. Ital. Suppl., 15, 176
Kuraszkiewicz J. et al., 2009a, ApJ, 692, 1143
Kuraszkiewicz J., Wilkes B. J., Schmidt G., Smith P. S., Cutri R., Czerny B., 2009b, ApJ, 692, 1180
LaMassa S. M., Heckman T. M., Ptak A., Martins L., Wild V., Sonnentrucker P., 2010, ApJ, 720, 786
Low F. J., Cutri R. M., Huchra J. P., Kleinmann S. G., 1988, ApJ, 327, 41
Marble A. R., Hines C., Schmidt G. D., Smith P. S., Surace J. A., Armus L., Cutri R. M., Nelson B. O., 2003, ApJ, 590, 707
Mathur S., 2000, MNRAS, 314, 17
McLure R. J., Dunlop J. S., 2001, MNRAS, 327, 199
Narayanan D. et al., 2006, ApJ, 642, 107
Nelson C. H., Whittle M., 1995, ApJS, 99, 67
Osterbrock D. E., Pogge R., 1985, ApJ, 297, 166
Peacock J. A., 1983, MNRAS, 202, 615
Pounds K. A., Done C., Osborne J. P., 1995, MNRAS, 277, 5
Reyes R. et al., 2008, AJ, 136, 2373
Robinson T. G., Tadhunter C. N., Axon D. J., Robinson A., 2000, MNRAS, 317, 922
Rodríguez Zaurín J., Tadhunter C. N., González Delgado R. M., 2009, MNRAS, 400, 1139
Rodríguez Zaurín J., Tadhunter C. N., González Delgado R. M., 2010, MNRAS, 403, 1317
Rose M., Tadhunter C. N., Holt J., Ramos Almeida C., Littlefair S. P., 2011, MNRAS, 414, 3360
Sarzi M. et al., 2006, MNRAS, 366, 1151
Schlegel D. J., Finkbeiner D. P., Davis M., 1998, ApJ, 500, 525
Schmidt M., Green R. F., 1983, ApJ, 269, 352
Seaton M. J., 1979, MNRAS, 187, 73
Shields G. A., Bonning E. W., 2008, ApJ, 682, 758
Shi Y. et al., 2007, ApJ, 669, 841
Smith P. S., Schmidt G. D., Hines D. C., Cutri R. M., Nelson B. O., 2002, ApJ, 569, 23
Spergel D. N. et al., 2003, ApJS, 148, 175
Tadhunter C., Wills K., Morganti R., Oosterloo T., Dickson R., 2001, MNRAS, 327, 227
Tadhunter C., Robinson T. G., González Delgado R. M., Wills K., Morganti R., 2005, MNRAS, 356, 480
Urrutia T., Lacy M., Becker R. H., 2008, ApJ, 674, 80
Urrutia T., Becker R. H., White R. L., Glikman E., Lacy M., Hodge J., Gregg M. D., 2009, ApJ, 698, 1095
Urrutia T., Lacy M., Spoon H., Glikman E., Petric A., Schulz B., 2012, ApJ, 757, 125
Véron-Cetty M.-P., Véron P., Gonçalves A. C., 2001, A&A, 372, 730
Webster R. L., Francis P. J., Peterson B. A., Drinkwater M. J., Masci F. J., 1995, Nat, 375, 469
Weymann R. J., Morris S. L., Foltz C. B., Hewett P. C., 1991, ApJ, 373, 23
Whittle M., 1985, MNRAS, 213, 1
Wilkes B. J., Schmidt G. D., Cutri R. M., Ghosh H., Hines D. C., Nelson B., Smith P. S., 2002, ApJ, 564, 65
York D. G. et al., 2000, AJ, 120, 1579
Zakamska N. L. et al., 2003, AJ, 126, 2144
Zhou H., Wang T., Yuan W., Lu H., Dong X., Wang J., Lu Y., 2006, ApJS, 166, 128

APPENDIX A: INDIVIDUAL PROPERTIES

J0221+13 is classified as an intermediate-type AGN (type 1.8) in both Smith et al. (2002) and Kuraszkiewicz et al. (2009a,b), however, our classification is consistent with the findings of Hutchings et al. (2003): a type 2 AGN. Such a difference can be explained by the difference in S/N between the spectra used to identify the AGN type.

J0306−05: while we find no evidence of broad-line emission in J0306−05, Hutchings et al. (2003) classify this object as a type 1 AGN.

J0312+07 is a type 1 Seyfert galaxy with $J - K_S = 1.98$. A companion object is detected on the 2D spectrum at a distance of $\sim$400 $\pm$ 80 kpc from the nucleus of J0312+07 (see Fig. A1). Interestingly, the continuum of this companion appears redder than the continuum of J0312+07. It is possible that the companion is interacting with the host galaxy of J0312+07, implying that J0312+07 may be a young AGN triggered in a recent merger. By measuring the difference in redshift in the Hα emission between J0312+07 and the companion galaxy, we have found that the companion is shifted by -240 ± 20 km s^{-1} relative to the rest frame of J0312+07. Therefore, we can reasonably argue that J0312+07 is in an interacting system.

J0400+05 is a type 1 quasar with $J - K_S = 2.00$. J0400+05 is the only object in the 2MASS sample with a detectable absorption feature for Mg II]$\lambda\lambda$2796, 2802. Fig. A2 shows the fit to the Mg II] absorption feature. From this fit we deduce that the absorption feature is blueshifted by 1200 $\pm$ 160 km s^{-1} relative to the rest frame of the 0400+05 narrow-line emission, and has a velocity width of 1510 $\pm$ 120 km s^{-1} (FWHM). These properties fall short of the LoBAL properties found for the objects in the Urrutia et al. (2009) and Glikman et al. (2012) samples because BAL objects are defined to be blueshifted by $\sim$3000–25000 km s^{-1} and have FWHM $>$ 2000 km s^1 (Weymann et al. 1991).

As well as absorption lines, the continuum of this object has an unusual shape which includes an unidentified, broad emission feature between 4200 and 5200 Å in the rest frame (see Fig. 1). In addition, the BLR Balmer emission in J0400+05 is significantly blueshifted by -2870 ± 160 km s^{-1} relative to the NLR emission. Such shifts in the BLR are predicted for the recoils ('kicks') that result from the merger of two black holes (Shields & Bonning 2008). The magnitude of the kick can be large: Dain, Lousto & Zlochower (2008) have computed kicks of up to 3300 km s^{-1}, but the most extreme kicks require black hole binaries of equal mass and spin, where the spins are extremely high. We further note that J0400+05 has the highest virial black hole mass calculated for the 2MASS sample. We note that Hutchings et al. (2003) do not detect the presence of the shifted broad-line emission in J0400+05; they classify this object as a type 2 AGN.

J1006+41: Hutchings et al. (2003) do not detect the presence of broad-line emission in J1006+41, whereas we detect broad-line emission in Hα and Fe II.

J1040+59 is a type 1 Seyfert galaxy with $J - K_S = 3.02$ – far higher than the median NIR colour of the sample. In addition to

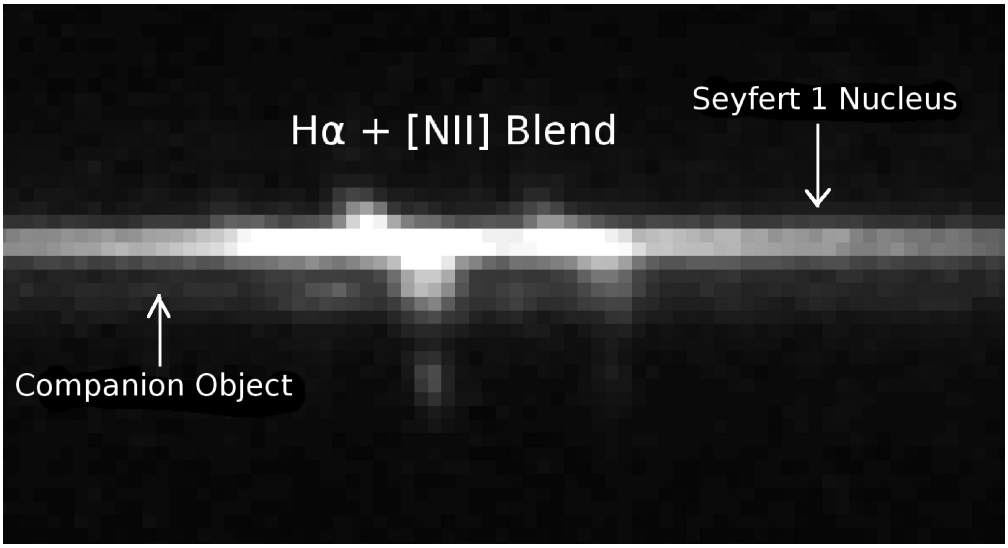

Figure A1. A section of the 2D WHT of J0312+07, focusing on the Hα+[N II] blend. There are clearly two continua in the spectrum. The top continuum is the continuum of J0312+07. The bottom continuum is the companion continuum. In addition, a nuclear velocity gradient in the Hα+[N II] blend.

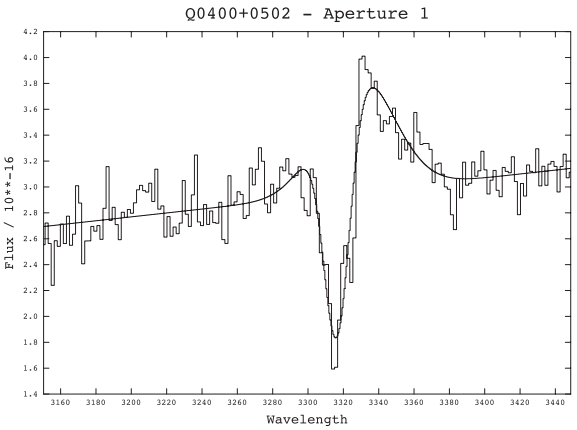

Figure A2. The Gaussian fit to the Mg II]$\lambda\lambda$2798, 2802 absorption and emission features. Note that both the Mg II] absorption and emission features overlap, making it difficult to obtain accurate measurements of the absorption/emission-line properties.

its unusually red $J - K_S$ colour, the optical continuum of this object rises more steeply to the red colour than any other object in the sample. Its shape is reminiscent of the object PKS 1549−79 which also has extremely red colours ($J - K_S = 2.82$; see Bellamy et al. 2003; Holt et al. 2006). PKS 1549−79 is believed to be a quasar which is enshrouded in a cocoon of natal gas and dust which is supplied by a recent merger (Tadhunter et al. 2001; Holt et al. 2006). J1040+59 also features in the Glikman et al. (2007) sample. Consistent with our results, while Glikman et al. (2007) found that J1040+59, and many of their objects, are sufficiently extinguished such that the broad Balmer emission lines are not present at optical wavelengths, broad Paschen lines are detected in the NIR.

J1057−13: Hutchings et al. (2003) classify J1057−13 as a LINER/H II-type object. However, based on the BPT diagrams (see Figs 9–11), and presence of FHILs, we find clear evidence that the emission-line properties of J1057−13 are consistent with those of a Seyfert-type AGN.

J1131+16 is a type 2 quasar with $J - K_S = 2.15$. This object has an unusually rich spectrum of FHILs, which are strong compared to the [O III]λ5007 line, and has been studied in detail by Rose et al. (2011). We believe that the unusual strengths of the FHILs in this object are due to a specific viewing angle of the far wall of the torus, coupled with a lack of dust on larger scales that might otherwise obscure our view of the torus. The spectrum of the hot dust emission ($\sim$1500 K) is expected to peak at wavelengths similar to the *K* band. The enhanced flux in this band could be the explanation for the red $J - K_S$ colour observed for this object.

J1158−30: we note that Hutchings et al. (2003) classify J1158−30 as a type 1 AGN, but we see no evidence of broad-line emission in our spectra.

J1307+23 is a type 2 Seyfert galaxy/LINER with $J - K_S = 3.31$ (the reddest $J - K_S$ colour in the sample) and has one of the largest redshifts in the sample ($z = 0.274$). It is possible that this object is a genuine type 2 AGN in which the AGN is subject to extremely high levels of extinction because the torus is viewed close to edge on, but due to the larger scale of the NLR, shows very little evidence for dust extinction in the narrow Balmer decrements. However, both Smith et al. (2002) and Hutchings et al. (2003) report the presence of broad-line emission in J1307+23, inconsistent with our analysis of its spectrum. On the other hand, we note that, like us, Kuraszkiewicz et al. (2009a,b) classify this object as a type 2 object.

J1321+13: like J1057−13, Hutchings et al. (2003) classify J1321+13 as a LINER/H II-type object. Again, based on the BPT diagrams (see Figs 9–11), and the detection of FHILs, we find that the emission-line properties of J1321+13 are consistent with those of a Seyfert-type AGN.

J1637+25 is classified as an intermediate-type AGN in both Smith et al. 2002 (type 1.9) and Kuraszkiewicz et al. 2009a,b (type 1.5), however, our classification is consistent with the finding of Hutchings et al. (2003) that this object is a type 2 AGN.

J2124−17 is a type 1 quasar with $J - K_S = 2.37$. Based on the visual inspection of the optical spectrum, this object appears to have an optical SED that is typical of UV-/optical-selected type 1 quasars. Another notable property of this object is that it has the strongest Fe II emission of all of the red 2MASS sample. However,

a single Gaussian fit to the Hβ emission line gives a velocity width FWHM of 2040 ± 30 km s^{-1} – which is higher than expected for a NLS1 (FWHM < 2000 km s^{-1}).

Another interesting property of this object is that it has been previously identified as an ULIRG (Kim & Sanders 1998). Indeed, this object, along with further 25 ULIRGs, is studied in more detail in Rodríguez Zaurín et al. (2009) and Rodríguez Zaurín, Tadhunter & González Delgado (2010).

A note on the comparison of classifications with other work. Most of the observed differences between AGN classifications noted in this Appendix can be explained by differences in S/N between the studies, or by differences in the method used to fit the Hα+[N II] blend of the observations, particularly for objects with weak broad lines, or classified as LINER/intermediate types.

This paper has been typeset from a TEX/LATEX file prepared by the author.